


## Measurement of an eddy diffusivity for chaotic electroconvection using combined computational and experimental techniques

Arunraj Balaji-Wright <sup>\*</sup>

*Department of Mechanical Engineering, Stanford University, Stanford, California 94305, USA*

Felix Stockmeier <sup>\*</sup>

*Chemical Process Engineering AVT.CVT, RWTH Aachen University, 52074 Aachen, Germany  
and DWI—Leibniz–Institute for Interactive Materials, 52074 Aachen, Germany*

Richard Dunkel 

*Chemical Process Engineering AVT.CVT, RWTH Aachen University, 52074 Aachen, Germany*

Matthias Wessling<sup>†</sup>

*Chemical Process Engineering AVT.CVT, RWTH Aachen University, 52074 Aachen, Germany  
and DWI—Leibniz–Institute for Interactive Materials, 52074 Aachen, Germany*

Ali Mani<sup>‡</sup>

*Department of Mechanical Engineering, Stanford University, Stanford, California 94305, USA*



(Received 15 August 2023; accepted 14 December 2023; published 23 February 2024)

The coupling between ion transport, fluid flow, and electrostatics may give rise to electroconvection, a physical phenomenon in which the buildup of charge near selective surfaces leads to hydrodynamic instability, eventually transitioning to an unsteady and chaotic flow. Though electroconvection contains a wide range of spatiotemporal scales, averaging of the ion concentration, velocity, and electric potential fields may produce a lower-dimensional and smoother representation while still capturing the essential performance metrics: ion current density and mean applied voltage, for example. The Poisson–Nernst–Planck–Stokes equations are known to capture the chaotic dynamics of electroconvection accurately. However, there is as of yet no way to directly compute the mean fields, since the application of the well-known Reynolds-averaging procedure leads to a closure problem. In this work, we combine the macroscopic forcing method, a numerical technique for measurement of closure operators in Reynolds-averaged equations, with high-fidelity experimental data to close the equations for the mean fields in chaotic electroconvection. We show that the unclosed fluxes in the Reynolds-averaged equations may be represented to the leading order as a gradient-diffusion term, with a spatially varying eddy diffusivity that we directly measure from experimental velocity fields. As a result, we are able to directly solve for the mean ion concentration and electric potential fields by supplementing the 1D Poisson–Nernst–Planck equations with an eddy diffusivity that captures the averaged effects of mixing due to chaotic, 3D electroconvection. The resulting current-voltage curve exhibits strong agreement with experiments. Our method allows for

---

<sup>\*</sup>These authors contributed equally to this work.

<sup>†</sup>manuscripts.cvt@avt.rwth-aachen.de

<sup>‡</sup>alimani@stanford.edu

the study of electroconvection with orders-of-magnitude cost savings by obviating the need for expensive direct numerical simulations. Additionally, our measured eddy diffusivity profiles provide a benchmark for the development of stand-alone reduced-order models of electroconvection.

DOI: [10.1103/PhysRevFluids.9.023701](https://doi.org/10.1103/PhysRevFluids.9.023701)

## I. INTRODUCTION

The problem of coupled ion transport and fluid flow appears in practical systems across a wide variety of applications. Electrodialysis [1], a process in which applied electric fields are used in conjunction with ion-selective membranes to remove ions from an electrolyte, is relevant in water desalination [2], industrial and municipal wastewater treatment [3], industrial chemical separations [4], and food processing [5]. Similarly rich physics are found in electrodeposition, where the coupling between electrolyte flow and surface morphology has long been known [6,7]. A contemporary application of crucial significance is batteries, where dendrite formation is substantially influenced by electroconvective flows [8–11].

The focus of this work is electroconvection. In contrast to the branch of electrohydrodynamics (EHD) concerning coupled ion and electrolyte transport in weakly conducting fluids [12,13], this work is squarely centered in the realm of electrokinetics, where electrolytes are taken to contain a large number of charged ions of both signs [14,15]. In EHD, charge is distributed along fluid interfaces, but current is allowed to pass through the fluid by means of a small and constant Ohmic conductivity. In electrokinetics, however, relatively large ion concentrations are present throughout the fluid, allowing for a finite net charge density and enabling bulk electric forcing of the electrolyte in the presence of electric fields and salinity gradients.

Consider a simple electrodialysis cell in which current is driven through a cation–exchange–membrane by an applied electric field. The current–voltage curve (or  $j$ - $V$  curve) of such a system typically exhibits three regions: (i) an Ohmic region, in which the current–voltage relation is linear, (ii) a limiting region, in which concentration polarization leads to saturation of the current at a value known as the limiting current, and (iii) an overlimiting region, in which the current again increases with voltage and begins to exhibit unsteady, chaotic fluctuations [16]. The overlimiting phenomenon was shown to result from chaotic, electrically driven convection, which mixes the electrolyte and helps mitigate the ion depletion caused by concentration polarization [17–19].

Various methods have since been employed to investigate electroconvection [20–23], including early theoretical works focused on the instability at the root of the phenomenon. Notably, Rubinstein and Zaltzman published a series of studies in which they applied the method of matched asymptotic expansions and stability analyses to develop a mathematical description of the electroconvective instability [24–26]. In the underlimiting regime, the system may be described by “outer” and “inner” zones. Most of the bulk falls into the former category, which is largely electroneutral. The inner zone, located adjacent to the ion–selective membrane, is a highly charged region governed by Boltzmann equilibrium. This inner zone, the electric double layer (EDL), has a thickness given by the Debye length,

$$\lambda_D = \sqrt{\frac{\epsilon_0 \epsilon_R k_B T}{2z^2 e^2 c_0}}, \quad (1)$$

which, for aqueous systems with electrolyte concentrations on the order  $c_0 \approx 1 \text{ mmolL}^{-1}$ , produces a length scale of  $\lambda_D \approx O(10 \text{ nm})$ . Here,  $\epsilon_0$  is the vacuum permittivity,  $\epsilon_R$  is the relative permittivity of the electrolyte,  $k_B$  is Boltzmann’s constant,  $T$  is the solution temperature,  $z$  is the valence of a binary electrolyte, and  $e$  is the fundamental charge. Beginning in the limiting regime, a new zone appears in between the two mentioned previously. Referred to as the extended space charge (ESC) layer [27], this zone is neither electroneutral nor in Boltzmann equilibrium. In the presence of

tangential electric fields (e.g., near curved surfaces), the electrolyte may exhibit an asymptotically zero-thickness slip velocity with respect to the membrane surface. Dukhin categorized the slipping phenomenon as either “of the first kind” or “of the second kind” depending on whether it resulted from slip of the EDL or the ESC, respectively [28,29]. Rubinstein and Zaltzman’s work, however, addressed the problem of inherent stability of the quiescent electrolyte in the absence of applied tangential electric fields or curvature. Whereas instability was unlikely for realistic electrolytes (ionic species with realistic values of mass diffusivity) when considering only slip of the first kind [30], inclusion of the ESC layer (slip of the second kind) leads to instability behavior that compares well with experiments [31].

Experimental and computational works have since explored the full nonlinear evolution of electroconvection. A number of authors performed current/voltage measurements and 2D visualization of electrodialysis cells using tracer particles and fluorescent dyes, with or without the presence of crossflow [31–34]. There has also been recent interest in the 3D structure of electroconvective vortices, particularly concerning their interaction with crossflow [35,36] and spacers [37,38]. We particularly emphasize recent papers in which particle tracking velocimetry (PTV) has been used to measure the 3D velocity fields in electroconvection, allowing for detailed analysis of the instability in its incipient stage, the statistics of stationary electroconvection, and the associated energy spectra [39–41]—a depth of analysis that was previously limited to computational work based on direct numerical simulation (DNS) of the Poisson–Nernst–Planck–Stokes equations [42–47]. Several very recent works have focused on the effects of membrane heterogeneity, including variation in selectivity and geometric undulations [48–53]. Such factors strongly affect the nature of electroconvection, potentially increasing the current density compared to that of fully homogeneous membranes. Furthermore, various authors have investigated the coupling between electroconvection and other phenomena, including Rayleigh–Benard convection [54,55], viscoelasticity [9], imperfect membrane selectivity [56], and electrodeposition [8–11,57,58].

DNS of the Poisson–Nernst–Planck–Stokes system in the overlimiting regime is considerably expensive. Consider the nondimensional Debye length  $\epsilon_D = \lambda_D/L$ , where  $L$  corresponds to the width of the electrolyte reservoir (which is commonly taken to be the size of the computational domain). The cost of simulations scales inversely with this ratio of length scales, since it determines the number of mesh points required to span the largest length scale while also resolving the smallest feature. Realistic values may be as small as  $\epsilon_D = O(10^{-7})$  for  $1 \text{ molL}^{-1}$  electrolytes in a 1 mm cell. Prior EDL-resolving computational works have utilized choices of  $\epsilon_D$  ranging from  $\epsilon_D = 1 \times 10^{-2}$  to  $\epsilon_D = 1 \times 10^{-5}$  [35,42,43,45–47,54,59–67]. Of the works that performed 3D simulations, the smallest value considered was  $\epsilon_D = 5 \times 10^{-4}$ . Furthermore, it has been shown that the number of dimensions [47] and the nondimensional Debye length [60] can affect the dynamics of electroconvection quantitatively.

The motivation for this work comes from two observations. First, despite the chaotic fluctuation of the current density (or voltage, in the case of galvanostatic measurements) in strongly overlimiting cases, the mean current density and mean voltage are sufficient to predict the power usage and ion exchange rate for the design of practical systems. The natural symmetry of planar electrochemical cells implies that averaging in the electrode/membrane-parallel directions is appropriate, yielding a smooth, 1D representation of the concentration and electric potential fields [45,47]. Averaging in time may also be performed for practical systems operating in a stationary state. This smooth and lower-dimensional representation alone—not the detailed fluctuations contained in the unsteady, chaotic 3D solution—is sufficient to compute the desired mean quantities. Second, a demonstrably accurate model for chaotic electroconvection exists in the form of the Poisson–Nernst–Planck–Stokes equations, but determination of mean quantities through this route requires expensive DNS.

Prior work has not yet yielded a method for direct computation of the mean fields without the need for DNS. Cai and coauthors utilized deep learning to demonstrate a data-assimilation framework for nonchaotic electroconvection, but their primary goal was prediction of the full electroconvection fields based on partial measurements of one of the fields [68]. In a recent work, Guan

and coauthors developed a sparse nonlinear model for chaotic electroconvection during unipolar charge injection in EHD, wherein a regression-based method is used to predict the nonlinear evolution of the coherent structures associated with the first few proper-orthogonal-decomposition (POD) modes of the charge density fields [69]. By enforcing phase-space symmetries of the POD coefficients as part of the regression, the authors find agreement between the sparse nonlinear model and POD analysis of the DNS results. Though it is conceivable to apply the same method to electrokinetic flows, it is unclear how many modes are required to accurately represent quantities like the current density. Additionally, whereas Guan and coauthors seek to reproduce the chaotic dynamics accurately, we are chiefly motivated to determine the time- and space-averaged effects of the underlying chaotic dynamics. Thus, we now introduce the methodology used in this work to enable direct computation of the mean fields.

Since the techniques used in this work are drawn from a different field of study, we briefly introduce an analogous problem in which a similar dilemma appears—scalar mixing in turbulent flows [70]. At high Reynolds numbers, the Navier–Stokes equations admit chaotic solutions in which velocity fields exhibit spatiotemporal fluctuations with broadband spectra. Fine-scale eddies are responsible for mixing solute dissolved in the fluid, but the mean velocity and concentration fields are of considerable interest in practical applications. This gave rise to the Reynolds-averaging procedure, whereby one may derive equations that directly govern the evolution of mean fields. Some form of modeling is required to close the nonlinear terms in these equations, whether algebraic in form or comprising additional transport equations. Two prior works have recognized this analogy in the context of EHD [71] and electrokinetics [45]. In the latter, Druzgalski and co-authors derive Reynolds-averaged analogs of the Poisson–Nernst–Planck–Stokes equations in the course of analyzing their DNS of the system, demonstrating the presence of two unclosed terms: one resulting from advection and the other from electromigration. In that work and in a followup [47], the authors demonstrated that the advection-related term is dominant in the bulk—as may be intuited since the bulk is largely electroneutral. Thus, closure of this advection term in particular appears to be a priority.

Mani and Park introduced the macroscopic forcing method (MFM) within the context of Reynolds-averaged Navier Stokes (RANS) modeling of turbulent transport, as a tool for the evaluation of differential operators to close the averaged equations [72]. Mirroring their terminology, we refer to the chaotically fluctuating fields as “microscopic” fields and the averaged fields as “macroscopic” fields. A similar distinction is drawn between the microscopic and macroscopic equations. Using MFM, it is possible to determine a macroscopic representation of transport due to microscopic fluctuations by examining how solutions to the microscopic equations respond to various imposed forcing terms. In the original work, Mani and Park are able to compute general (i.e., spatiotemporally nonlocal and anisotropic) operators to close the macroscopic equations in a number of example scalar- and momentum-transport problems. Given space-time-resolved velocity fields, the MFM procedure may be used to determine a corresponding closure operator in the form of an eddy diffusivity (which, in its most general form, is a tensorial kernel that captures spatiotemporal nonlocality and anisotropy).

However, the conventional MFM procedure entails significant computational cost, since 3D DNS results are required as inputs to the procedure. Considering that each simulation would need to be performed with a realistic Debye length, the prospect of performing MFM on an electroconvection system quickly becomes intractable. Therefore, as opposed to using DNS fields as inputs to the procedure, we incorporate 3D, time-resolved velocity field measurements from particle tracking velocimetry (PTV) experiments. The experimentally measured velocity fields are fed into a variant of the MFM procedure referred to as the inverse macroscopic forcing method (IMFM), which is designed to efficiently compute spatial moments of the eddy diffusivity kernel using a single forced simulation per moment.

Thus, by combining novel computational and experimental techniques, we circumvent the tractability problem associated with MFM and measure a closure operator for the dominant unclosed term in the Reynolds-averaged Poisson–Nernst–Planck–Stokes equations. As we will show, transport

due to microscopic electroconvection may be represented to leading order as a gradient-diffusion term in the macroscopic space. Furthermore, we use our combined numerical and experimental technique to directly measure the corresponding eddy diffusivity. Finally, we show that *a posteriori* analysis of our closure operator exhibits excellent agreement with experiments.

The rest of this paper is organized as follows: In Sec. II, we introduce the general framework for our reduced-order model. The application of Reynolds averaging to the Poisson–Nernst–Planck–Stokes equations leads to a closure problem, but we demonstrate how one may measure the leading order macroscopic representation of the unclosed terms: namely, as a gradient diffusion term with a spatially varying eddy diffusivity. In Sec. III, we describe the experimental measurement of 3D, time-resolved velocity fields using PTV. In Sec. IV, we display the measured eddy diffusivity profiles and we demonstrate their *a posteriori* accuracy by performing simulations of the closed macroscopic equations. Two approaches are shown: First, we use the exact measurements of diffusivity profiles for the cases corresponding to experiments. Second, we propose a voltage-dependent form that allows interpolation between the applied voltage values for which experimental measurements are available. Finally, in Sec. V, we offer a discussion of the results and concluding remarks.

## II. MODEL FRAMEWORK

The objective of this section is developing the framework for a model to represent mean transport due to chaotic electroconvection. Although Reynolds’s averaging is a promising approach, the associated closure problem must be addressed. We show rigorously that the unclosed flux can be represented to leading order as a gradient-diffusion term with a spatially varying diffusivity coefficient, and we outline a method by which this eddy diffusivity can be measured from experimental data. This section is subdivided into two parts: The first part rigorously defines the microscopic and macroscopic equations for electroconvection, revealing the unclosed terms in the macroscopic equations. The second part introduces the MFM procedure and explains how velocity fields from experiments are incorporated therein, bypassing computationally intractable steps and yielding a measurement of the eddy diffusivity.

### A. Overview of microscopic and macroscopic equations

We begin with the microscopic equations, which capture the full, space–time–resolved physics of electroconvection at continuum scales. It is well known that the combined Poisson–Nernst–Planck–Stokes equations can accurately model electrolyte flow and ion transport in systems with electroconvection [20,25,26,45,47]:

$$\frac{\partial c_i}{\partial t} + \vec{\nabla} \cdot \vec{F}_i = 0, \quad (2)$$

$$\vec{F}_i = \vec{u}c_i - D_i\vec{\nabla}c_i - D_i\frac{z_ie}{k_B T}c_i\vec{\nabla}\phi, \quad (3)$$

$$-\varepsilon_0\varepsilon_r\nabla^2\phi = \sum_i e z_i c_i, \quad (4)$$

$$\frac{\partial \vec{u}_i}{\partial t} = -\frac{1}{\rho}\vec{\nabla}p + \nu\nabla^2\vec{u} - \frac{1}{\rho}\sum_i e z_i c_i\vec{\nabla}\phi, \quad (5)$$

and

$$\vec{\nabla} \cdot \vec{u} = 0. \quad (6)$$

Together, Eqs. (2) and (3) describe ion transport due to advection, diffusion, and electromigration of some species  $i$  whose concentration is given by  $c_i$ . Equation 3 is the Nernst–Planck flux supplemented with an advection term. Note that Einstein’s relation has been used to write the electric mobility  $\mu_i$  in terms of mass diffusivity  $D_i$ :  $\mu_i = D_i z_i e / k_B T$ . Equation 4 is Poisson’s equation for the

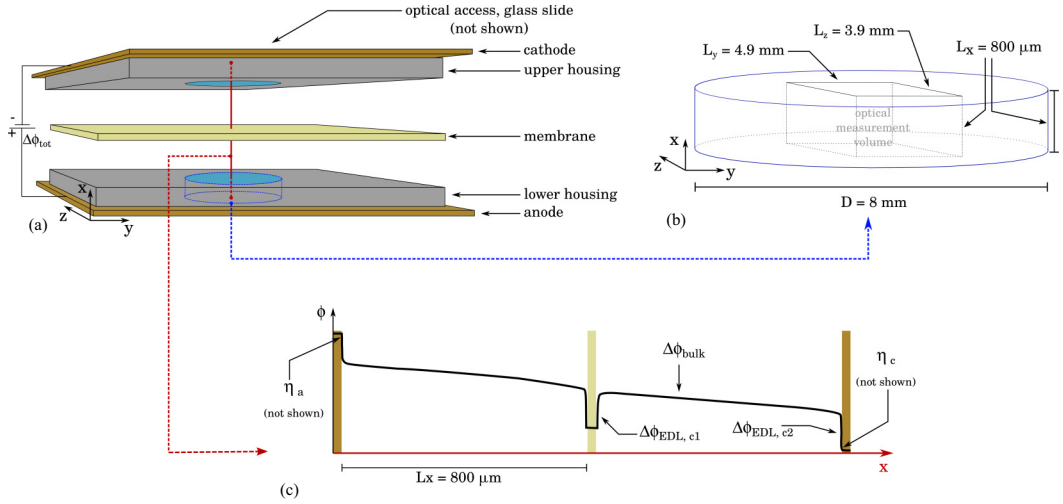


FIG. 1. Note: Figure not drawn to scale. (a) An exploded schematic of the experimental apparatus, showing two electrolyte reservoirs and the cation-selective membrane sandwiched between copper electrodes. (b) An inset of the anolyte chamber, showing the volume over which PTV is performed and velocity fields are measured in experiments. This optical measurement volume is also the domain for the computational component of this study. (c) A representative sketch of electric potential along the red reference line shown in panel (a), indicating potential drops that occur at various locations in the electrochemical cell. Additional details regarding the apparatus may be found in Ref. [41].

electric potential,  $\phi$ . Given the low Reynolds numbers at which electroconvection typically occurs, Eqs. (5) and (6) are the Stokes equations for the electrolyte velocity,  $\vec{u}$ , and the hydrodynamic pressure,  $p$ . Note the presence of an electric body force, the last term in Eq. (5). The constants  $D_i$ ,  $z_i$ ,  $e$ ,  $k_B$ ,  $T$ ,  $\epsilon_0$ ,  $\epsilon_R$ ,  $\rho$ , and  $\nu$ , are ion mass diffusivity, ion valence, elementary charge, Boltzmann's constant, system temperature, vacuum permittivity, electrolyte relative permittivity, electrolyte mass density, and electrolyte kinematic viscosity, respectively.

The conventional DNS approach would entail discretizing and solving the microscopic [Eqs. (2) to (6)] with the appropriate boundary conditions, yielding the microscopic fields  $c_i$ ,  $\phi$ ,  $\vec{u}$ , and  $p$ . Instead, we seek to directly predict the macroscopic fields, which are smoother and occupy a lower-dimensional space.

Averaging is proposed as the means of analytically bridging the microscopic and macroscopic spaces, but the specific type of averaging to be employed—spatial, temporal, or ensemble—depends on the specific problem geometry. Therefore, we now introduce in Fig. 1 the geometry that will be used in both the computational and experimental components of this study. The full electrochemical cell is shown in panel (a); both the anolyte and catholyte chambers are initially filled with a  $1 \text{ mmolL}^{-1}$  solution of copper sulfate. Since electroconvection is only expected in the anolyte chamber, we restrict our analysis to this region alone. Note in panel (b) the rectilinear 3D domain with dimensions  $L_x$ ,  $L_y$ , and  $L_z$ , located within the anolyte chamber and bounded below and above by a copper electrode and cation-exchange-membrane, respectively.

The aspect ratio of the anolyte chamber shown in Fig. 1(b) ensures that assuming statistical homogeneity in the  $y$  and  $z$  dimensions is appropriate everywhere except for a thin zone near the edges of the chamber. This suggests that a 1D representation varying only in  $x$  is appropriate after averaging in the other spatial dimensions. Additionally, for a fixed applied electric potential or current, the system is expected to reach a statistically stationary state once electroconvection is established. Consequently, for some microscopic field  $f$ , we introduce the macroscopic



field  $\bar{f}$  as

$$\bar{f}(x) = \frac{1}{T} \int_0^T \frac{1}{L_z} \int_0^{L_z} \frac{1}{L_y} \int_0^{L_y} f(x, y, z, t) dy dz dt. \quad (7)$$

The averaging operation performed in Eq. (7) can be viewed as a projection from the microscopic space inhabited by  $f(x, y, z, t)$  to the macroscopic space inhabited by  $\bar{f}(x)$ . The duration of measurement  $T$  must be much longer than the time scale of fluctuations in electroconvection. Similarly,  $L_y$  and  $L_z$  must be larger than the size of vortices in the flow.

We now seek to derive a set of macroscopic analogs of Eqs. (2) to (6) that will govern the evolution of macroscopic fields. We begin with the velocity field, immediately realizing a key feature of working in the macroscopic space:  $\bar{u} = 0$ , which follows from continuity [Eq. (6)] in addition to the no-penetration boundary conditions at the electrode/membrane and statistical homogeneity/symmetry in the  $y$  and  $z$  directions. Therefore, we do not need to develop macroscopic analogs for Eqs. (5) and (6). Treatment of the remaining equations requires the introduction of Reynolds' decomposition of fields into mean and fluctuating components:  $f' \equiv f - \bar{f}$ , such that  $f = \bar{f} + f'$  [70]. Applying Reynolds' decomposition and averaging to Eqs. (2) to (4), we arrive at

$$\frac{\partial \bar{c}_i}{\partial t} + \frac{\partial}{\partial x} \left( -D_i \frac{\partial \bar{c}_i}{\partial x} - D_i \frac{z_i e}{k_B T} \bar{c}_i \frac{\partial \bar{\phi}}{\partial x} \right) = -\frac{\partial}{\partial x} \left( \overline{u'_x c'_i} - D_i \frac{z_i e}{k_B T} \overline{c'_i \frac{\partial \phi'}{\partial x}} \right) \quad (8)$$

and

$$-\varepsilon_0 \varepsilon_r \frac{\partial^2 \bar{\phi}}{\partial x^2} = \sum_i e z_i \bar{c}_i. \quad (9)$$

We have used the facts that differentiation in  $x$  commutes with the averaging operation defined in Equation 7 and that gradients in homogeneous dimensions are analytically zero for macroscopic quantities. The unsteady term has been retained despite temporal averaging because artificial time stepping will be used to compute the steady-state  $\bar{c}_i$  in Sec. IV B.

Note that Eq. (9) is expressed entirely in terms of the macroscopic variables  $\bar{\phi}$  and  $\bar{c}_i$ . Meanwhile, two unclosed terms—the first involving  $\overline{u'_x c'_i}$  and the second involving  $\overline{c'_i \partial \phi' / \partial x}$ —are present on the right side of Eq. (8). Prior *a priori* analysis of the unclosed terms in Eq. (8) for a similar system found that the first term  $\overline{u'_x c'_i}$  is dominant except in a thin region near the membrane [45,47]. To capture the leading-order physics, we focus our modeling efforts on the first term alone.

Physically, the first unclosed term in Eq. (8) represents the mean effect of mixing due to velocity field fluctuations. We will continue with our analysis in the limit of vanishing Debye length, assuming electroneutrality in regions with appreciable advective mixing. This simplification allows analysis of species transport via a single equation governing the behavior of an electroneutral salt, in which the only remaining terms are due to ambipolar diffusion and advection. In the next part, we determine the advective closure operator based on this transport equation for an electroneutral salt, and we assume that the same operator governs advective mixing for individual species in Eq. (8).

## B. MFM procedure with experimentally measured velocity fields

We now outline the MFM procedure. Whereas the conventional MFM technique would require velocity fields from 3D DNS simulations as inputs, we instead use the 3D, time-resolved velocity fields from experiments. Such a workaround is crucial, since full microscopic simulations using an accurate Debye length are prohibitively expensive [61].

As a first step, we reconsider Eqs. (2)–(4) in the limit of electroneutrality for a binary electrolyte, where we may take  $\sum_i z_i c_i = z_+ c_+ + z_- c_- = 0$ . The positive and negative subscript refer to the cation and anion, respectively. We aim to write a transport equation for  $c \equiv (z_+ c_+ - z_- c_-) / (z_+ - z_-)$ , which is the electroneutral salt concentration. For a binary and symmetric electrolyte, the electroneutral salt concentration is simply the arithmetic mean of the individual cation and

anion concentrations. Furthermore, considering the electroneutrality constraint, we may write that  $c = c_+ = c_-$  for a binary and symmetric electrolyte.

Utilizing the definition of  $c$  introduced above and the electroneutrality constraint, the individual ionic transport equations may be combined to eliminate the electric potential, yielding

$$\frac{\partial c}{\partial t} + \vec{\nabla} \cdot (\vec{u}c - D_A \vec{\nabla} c) = 0, \quad (10)$$

where the ambipolar diffusivity is given generally (i.e., for binary symmetric or binary asymmetric electrolytes) by  $D_A \equiv (z_+ - z_-)D_+D_-/(z_+D_+ - z_-D_-)$ . Finally, Reynolds averaging is performed to determine the macroscopic equation

$$\frac{\partial \bar{c}}{\partial t} - \frac{\partial}{\partial x} \left( D_A \frac{\partial \bar{c}}{\partial x} \right) = -\frac{\partial}{\partial x} (\overline{u'_x c'}). \quad (11)$$

Under the assumption of electroneutrality, the unclosed term in Eq. (11) is identical to the unclosed advection term appearing in Eq. (8). Therefore, we may use Eqs. (10) and (11) as the microscopic and macroscopic equations for the MFM procedure, and the resulting closure operator is expected to be valid for use in Eq. (8) as well.

Following Refs. [72,73], we introduce a general representation of the unclosed term in Eq. (11) by writing

$$-\overline{u'_x c'}(x) = \int_0^{L_x} \mathcal{D}(x, \tilde{x}) \frac{\partial \bar{c}}{\partial x} \Big|_{\tilde{x}} d\tilde{x}. \quad (12)$$

The diffusivity kernel  $\mathcal{D}(x, \tilde{x})$  quantifies the influence of  $\partial \bar{c} / \partial x|_{\tilde{x}}$ , the macroscopic scalar gradient at location  $\tilde{x}$ , on the closure flux at location  $x$ . We emphasize that this representation does not impose physical constraints on the closure flux, since we have not yet specified the diffusivity kernel  $\mathcal{D}$ . In fact, the primary goal of the MFM method is measurement of the kernel based on the inherent details of the microscopic fields.

Following Ref. [72], Eq. (12) can be represented using the Kramers–Moyal expansions by writing  $\partial \bar{c} / \partial x|_{\tilde{x}}$  in terms of its Taylor series expansion around  $x$ . This results in

$$-\overline{u'_x c'}(x) = D^0(x) \frac{\partial \bar{c}}{\partial x} + D^1(x) \frac{\partial^2 \bar{c}}{\partial x^2} + D^2(x) \frac{\partial^3 \bar{c}}{\partial x^3} + \dots, \quad (13)$$

where  $D^j(x)$  is the  $j$ th spatial moment of  $\mathcal{D}(x, \tilde{x})$  in the  $\tilde{x}$  space, weighted by the inverse factorial of  $j$ :

$$D^j(x) = \int_0^{L_x} \frac{(\tilde{x} - x)^j}{j!} \mathcal{D}(x, \tilde{x}) d\tilde{x}. \quad (14)$$

Within this context, characterization of the advective closure operator is reduced to quantification of each  $D^j$ . Mani and Park demonstrated that each  $D^j$  may be determined through a procedure they refer to as the Inverse Macroscopic Forcing Method (IMFM). As explained in the original work, IMFM differs from the general MFM method insofar as its objective is to utilize a specific forcing function to determine an individual moment of the diffusivity kernel per forced simulation, as opposed to using a large sample of forcing functions to determine the entire kernel element by element.

While IMFM may be used to determine an arbitrary number of the  $D^j$  fields, we utilize this technique to only compute  $D^0(x)$ , approximating the closure operator by only retaining the leading order term in Eq. (13). This type of truncation yields the Boussinesq–limit eddy diffusivity, in which  $\mathcal{D}(x, \tilde{x})$  is implied to be a Dirac delta function centered around  $\tilde{x} = x$ , limiting the sensitivity of the closure flux to local mean gradients [72]. This approximation is formally valid when there is separation in magnitude between the macroscopic and microscopic length scales. However, our analyses of closures in other problems suggests that even without a clear separation of scales, the



leading order term in Eq. (13) represents the dominant portion of the total closure flux [72,74–76]. As shown in Sec. IV, the same approximation for the problem considered here leads to reasonable predictions of system-level behavior compared to experiments.

Following the IMFM procedure [72],  $D^0$  may be determined by performing a forced simulation of Eq. (10) using

$$\frac{\partial c}{\partial t} + \vec{\nabla} \cdot (\vec{u}c - D_A \vec{\nabla} c) = s, \quad (15)$$

where  $s$  is a forcing term that belongs to the macroscopic space:  $\bar{s} = s$ . Here,  $s$  is purely a function of  $x$  and steady in time. We take the microscopic velocity field  $\vec{u}$  to be known in advance from experiments, as opposed to determining them through an expensive two-way coupled simulation with the momentum equations.

The goal of IMFM is to select a forcing function  $s(x)$  such that the resulting concentration field  $c$  will yield an average  $\bar{c}$  that matches a prespecified target profile  $\bar{c}_T(x)$ , thereby allowing for determination of individual moments of the diffusivity kernel. For example, say one chooses  $\bar{c}_T = x$  and simulates Eq. (15) using an  $s(x)$  that guarantees  $\bar{c} = \bar{c}_T(x) = x$ . Applying Eq. (13),  $D^0(x)$  is determined by computing  $-\overline{u'_x c'}$  from the resulting fields. In other words,  $D^0 = -\overline{u'_x c'}$  for this specific forced simulation. Similarly, higher order  $D^j$  may be successively computed by setting  $\bar{c}_T(x)$  equal to higher order polynomials and running additional simulations.

The  $s$  required to yield a target  $\bar{c}_T(x)$  is given by

$$s = \frac{\bar{c}_T - \bar{c}}{\Delta t} + \vec{\nabla} \cdot (\vec{u}\bar{c} - D_A \vec{\nabla} \bar{c}), \quad (16)$$

which is presented in the context of a temporal discretization with time step  $\Delta t$ . As previously described [72], this choice of  $s$  constrains the macroscopic concentration profile while permitting microscopic fluctuations.

Once  $D^0(x)$  is determined through forced simulation of Eqs. (15) and (16) using  $\bar{c}_T = x$ , we are left with a simple gradient–diffusion model for the mixing due to electroconvection, given by the leading order term in Eq. (13). The eddy diffusivity, given by  $D^0(x)$ , captures the leading–order mean effects of mixing due to chaotic velocity fields, and is a function of space that we directly measure from a combined numerical and experimental technique. Thus, we have provided a closure for the unclosed term in Eq. (11), and, as discussed, the same closure flux is expected to capture the leading order effect of the unclosed advection term in Eq. (8). Recall that of the two unclosed terms in Eq. (8), the advection term is dominant for a vast majority of the domain. Neglecting the other unclosed term, Eq. (8) may now be written in closed form as

$$\frac{\partial \bar{c}_i}{\partial t} + \frac{\partial}{\partial x} \left( -D_i \frac{\partial \bar{c}_i}{\partial x} - D_i \frac{z_i e}{k_B T} \bar{c}_i \frac{\partial \bar{\phi}}{\partial x} \right) = -\frac{\partial}{\partial x} \left[ -D^0(x) \frac{\partial \bar{c}_i}{\partial x} \right] \quad (17)$$

and solved in conjunction with Eq. (9).

### III. EXPERIMENTAL MEASUREMENT OF VELOCITY FIELDS

The primary objective of this section is describing the experiments in which 3D, time-resolved velocity fields are directly measured using PTV. As noted previously, these measured velocity fields allow us to eschew a DNS of the Poisson–Nernst–Planck–Stokes equations as a precursor to the MFM procedure, saving significantly on cost and circumventing the need to introduce artificially thickened electric double layers or other numerical tricks. Since the experimental procedure used here is the same as that described by Stockmeier and coauthors [40,41], we only offer a brief sketch of the relevant details here and refer readers to the original publications for a more exhaustive description.

An exploded view of the full electrochemical cell is shown in Fig. 1.

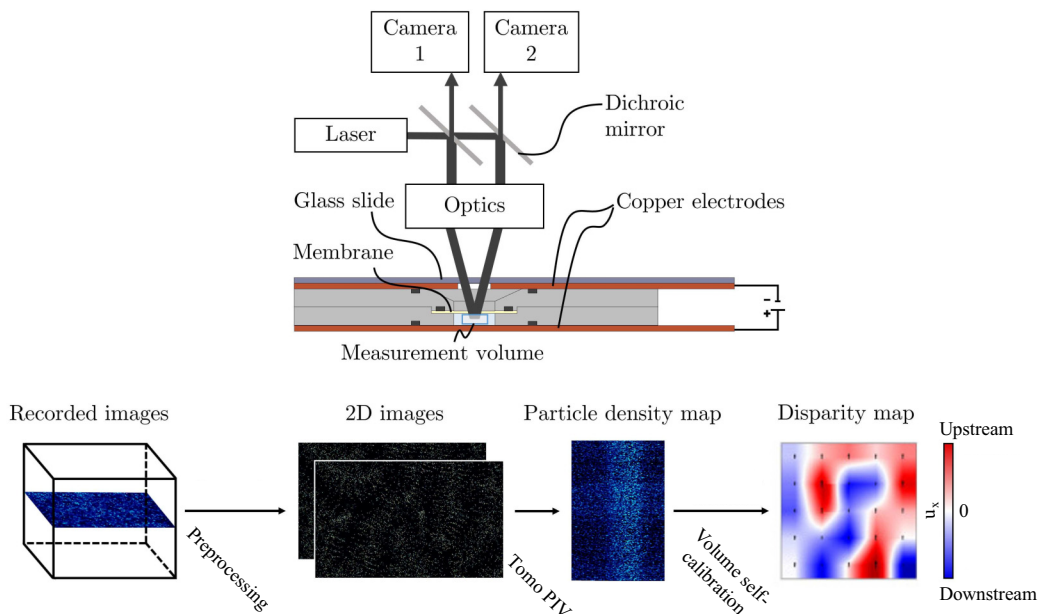


FIG. 2. Schematic of the experimental setup for stereo PTV. A laser illuminates the fluorescent tracer particles in the measurement volume, which are recorded by a stereo camera pair. The stereo images of the volume acquired over time are preprocessed to reduce noise and improve the visibility of particles. The spatial boundaries of the volume are then determined in the membrane-normal direction using tomographic PIV. In the last step, volume self-calibration is used to increase the accuracy of the calibration and to correct image distortion due to light refraction at the surface. Additional details may be found in the work by Stockmeier and coauthors [40,41]. Partially reprinted from Stockmeier *et al.*, “Direct 3D observation and unraveling of electroconvection phenomena during concentration polarization at ion-exchange membranes [40], with permission from Elsevier.

The center cation-exchange membrane (Nafion N117, Chemours, Wilmington, Delaware, USA), electrodes (copper,  $25\text{ mm} \times 75\text{ mm} \times 0.5\text{ mm}$ ), and 3D-printed housing parts form a pair of electrochemical half-cells. Both chambers are filled with a  $1\text{ mmolL}^{-1}$  solution of copper sulfate,  $\text{CuSO}_4$ , but the anolyte is seeded with inert, fluorescent polystyrene tracer particles (0.001 wt%,  $3.2\text{ }\mu\text{m}$  diameter, Thermo Scientific, Waltham, MA). The Zeta potential of the tracer particles was measured to be  $-14.9\text{ }\mu\text{V}$  using a Malvern Zetasizer Nano ZS (Malvern Panalytical Ltd). Due to their charge, the particles are influenced by the electric field. However, similar to prior experimental works [34,39], the velocity induced by electric fields is at least an order of magnitude smaller than that due to advection.

Details about the optical measurement setup are shown in Fig. 2. A stereo microscope (SteREO Discovery.V20, Carl Zeiss Microscopy Deutschland GmbH, Germany) with a  $1\times$  objective (Plan-Aprochromat  $1\times$ , Carl Zeiss Microscopy Deutschland GmbH, Germany) is focused within the optical measurement volume. A high-frequency Nd:YAG laser (532 nm, DM150, Photonics Industries International Inc.) illuminates the tracer particles, and their emitted fluorescent light is recorded by two high-speed cameras (Phantom VEO 710L, Vision Research Inc.). At a magnification of  $5.12\times$  with a half-way-closed aperture, it is possible to record the complete membrane-to-electrode distance. The particle tracks are processed in DaVis (version: 10.0.5.47779, LaVision GmbH, Göttingen, Germany), resulting in a velocity field with a size of  $4.9\text{ mm} \times 3.1\text{ mm} \times 0.8\text{ mm}$  and  $128\text{ px} \times 80\text{ px} \times 21\text{ px}$  resolution in space, and 20 Hz in time. Examples of the tracer particle paths and reconstructed Eulerian velocity fields are shown in Fig. 3.

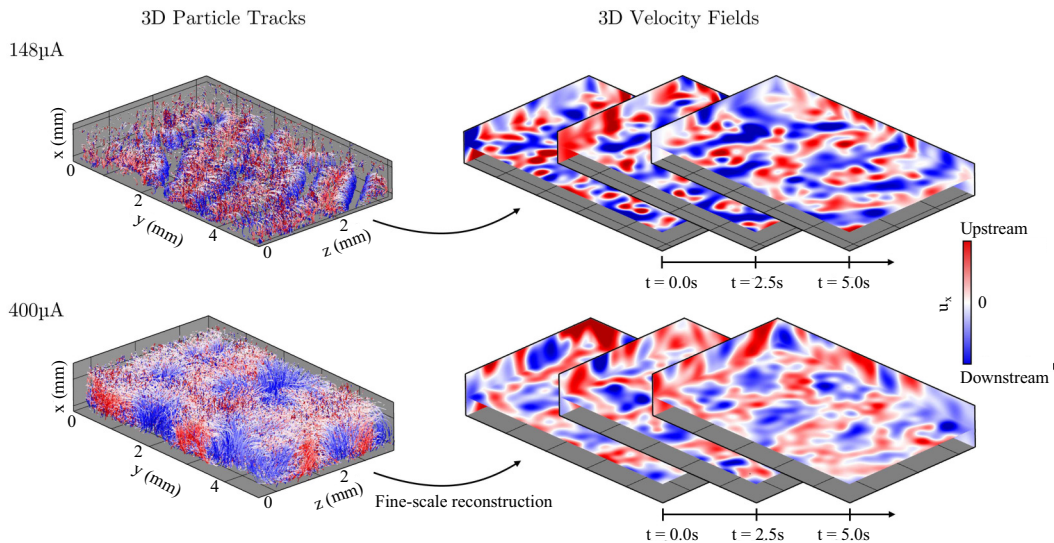


FIG. 3. Construction of 3D velocity fields from 3D particle tracks using the fine-scale reconstruction method. The colors indicate the velocity component in membrane-normal direction. Example cases are shown at applied DC current values of  $148 \mu\text{A}$  and  $400 \mu\text{A}$ , as indicated. Additional details may be found in the work by Stockmeier and coauthors [40,41].

During each experiment, a DC current is applied to the cell and the difference in electric potential between the electrodes is measured. Though the experiment is performed galvanostatically, measurements are taken when the applied electric potential reaches a statistically stationary state (details may be found in the original experimental work [40,41] and in other recent works that investigate the stationary portion of chronopotentiometric measurements [77,78]). We take the potential difference between electrodes,  $\Delta\phi_{\text{tot}}$ , to be a time-averaged value in the stationary state, allowing us to use a potentiostatic simulation approach in Sec. IV B.  $\Delta\phi_{\text{tot}}$  comprises all the contributions shown in Fig. 1(c). Meanwhile, the computational procedure will only include the anolyte region, since electroconvection only occurs in this half of the electrochemical cell. The potential difference across the anolyte—which we refer to simply as  $\Delta\phi$ —may be written as  $\Delta\phi = \Delta\phi_{\text{tot}} - \eta_a - \eta_c - \Delta\phi_{\text{EDL},c1} - \Delta\phi_{\text{EDL},c2} - \Delta\phi_{\text{bulk}}$ , where each of these components is shown in Fig. 1.

The overpotential  $\eta$  due to copper dissolution and deposition at the electrodes may be modeled using the Butler–Volmer equation as

$$i = i_0 \left[ \exp\left(\frac{\beta e}{k_B T} \eta\right) - \exp\left(\frac{(2 - \beta)e}{k_B T} \eta\right) \right], \quad (18)$$

where  $i$  is the current density,  $i_0$  is the exchange current density, and  $\beta = 0.5$  is the symmetry factor [79,80]. The mechanism shown in Eq. (18) may be adapted to both the anode and cathode, allowing for computation of  $\eta_a$  and  $\eta_c$  based on the measured mean current density. We adopt a value of  $i_0 = 3.7 \times 10^{-3} \text{ mAcm}^{-2}$ , based on the value measured for a copper electrode adjacent to  $0.5 \text{ molL}^{-1}$  copper sulfate solution [81], along with an analytical correction for the discrepancy in electrolyte concentration [79,80].

An Ohmic model is employed for the catholyte bulk using resistivity  $\rho_{\text{bulk}}$  and length  $L_{\text{bulk}}$  as

$$\Delta\phi_{\text{bulk}} = i\rho_{\text{bulk}}L_{\text{bulk}}. \quad (19)$$

Additionally, the total potential difference across both EDLs in the catholyte region is taken to be a constant. The values of  $\rho_{\text{bulk}}L_{\text{bulk}} = 8.11 \times 10^{-2} \Omega\text{m}^2$  and  $(\Delta\phi_{\text{EDL},c1} + \Delta\phi_{\text{EDL},c2}) = 8.93 \text{ mV}$  are determined based on comparison to 1D simulations of the Poisson–Nernst–Planck equations in the ohmic regime, where electroconvection is not expected and a 1D approach is justified. Thus, these two fitting parameters allow for matching of the conductivity and open-circuit-potential in the Ohmic regime (see the black and red curves in Fig. 11).

#### IV. MEASUREMENT AND EVALUATION OF EDDY DIFFUSIVITY

We remind readers that we concluded Sec. II with Eq. (17), which, in tandem with Eq. (9), constitutes a closed system of partial differential equations for the macroscopic  $\bar{c}_i$  and  $\bar{\phi}$  fields. We also described the procedure whereby the eddy diffusivity  $D^0(x)$  may be computed using the experimentally measured velocity fields. Consequently, this section is divided into two parts. In the first part, we describe our implementation of the MFM procedure and display the resulting eddy diffusivity profiles. Two approaches are shown: (i) We measure a separate eddy diffusivity profile for each value of  $\Delta\phi$  used in experiments. (ii) We propose a voltage-dependent profile that allows interpolation between the cases for which experimental measurements are available. In the second part, we evaluate *a posteriori* performance of the eddy diffusivity by directly solving the macroscopic equations for the mean fields and current density and comparing the results against experiments.

##### A. Measurement of eddy diffusivity

As described previously, measurement of  $D^0$  requires numerical solution of Eqs. (15) and (16) with the target mean concentration profile given by  $\bar{c}_T = x$ . The computational domain corresponds to the optical measurement volume shown in Fig. 1, which is a 3D, rectangular subregion of the anolyte chamber.

Generally, boundary conditions for  $c$  in the forced microscopic simulation should be consistent with the target profile  $\bar{c}_T$ . Therefore, Dirichlet conditions are used in  $x$ , corresponding to the linear profile given by  $\bar{c}_T = x$ . We exploit homogeneity in  $y$  and in  $z$  by choosing periodic boundary conditions in those dimensions. Strictly speaking, the experimentally measured velocity fields are not instantaneously periodic in the  $y$  and  $z$  dimensions, thereby inducing errors when periodic boundary conditions are used for the microscopic salt concentration field. However, we expect these errors to be confined to the near-boundary regions. Thus, the  $y$  and  $z$  averaging performed to compute  $D^0(x) = -(\overline{u'_x c'})$  will mitigate the influence thereof.

Note that the cell thickness  $L_x$  varies slightly from case to case due to changes in the experimental setup. Though we target  $L_x = 800 \mu\text{m}$  for each experiment, the cell assembly procedure does not guarantee enough precision to use the nominal value of  $L_x$  in the MFM procedure. Since the optical measurement and reconstruction procedure allows for measurement of the actual  $L_x$  for each experiment, we use the measured  $L_x$  value for each applied electric potential, as detailed in Table I.

TABLE I. Value of domain length,  $L_x$ , for each experimental case. Variation occurs due to imprecision in the cell construction process.

$\Delta\phi$	$L_x$
0.5347 V	729 $\mu\text{m}$
0.5572 V	614 $\mu\text{m}$
0.6343 V	614 $\mu\text{m}$
1.3341 V	614 $\mu\text{m}$
2.1051 V	729 $\mu\text{m}$
2.6134 V	729 $\mu\text{m}$
3.6780 V	803 $\mu\text{m}$

TABLE II. Values of physical constants used in the MFM procedure and in the subsequent simulation of the closed macroscopic equations.

Constant	Species	Value	Source
$D_i$	$\text{Cu}^{2+}$	$0.714 \times 10^{-9} \text{ m}^2\text{s}^{-1}$	[82]
	$\text{SO}_4^{2-}$	$1.065 \times 10^{-9} \text{ m}^2\text{s}^{-1}$	[82]
$z_i$	$\text{Cu}^{2+}$	+2	—
	$\text{SO}_4^{2-}$	-2	—
$D_A$	—	$0.855 \times 10^{-9} \text{ m}^2\text{s}^{-1}$	—
$e$	—	$1.602 \times 10^{-19} \text{ C}$	[82]
$k_B$	—	$1.380 \times 10^{-23} \text{ J K}^{-1}$	[82]
$T$	—	300 K	—
$\epsilon_0$	—	$8.85 \times 10^{-12} \text{ Fm}^{-1}$	[82]
$\epsilon_r$	—	80	[82]

Additionally, since the cation-selective membrane is not rigid, local pressure fluctuations may induce deformations in its shape. As a result, some points in space may be intermittently occupied by the membrane itself, leading to intermittency in the velocity measurements at those points. We neglect data at points for which velocity measurements are intermittent. Instead, we use linear interpolation between the adjacent boundary (where velocity is zero due to the no-slip condition) and the closest point in the domain that has velocity data available for every point in time.

The MFM procedure must be performed with sufficient spatial resolution to capture thin features that develop in the salt concentration field. Thus, each measured velocity field is linearly interpolated onto a staggered mesh with size  $84 \times 128 \times 128$ . Furthermore, the mesh is nonuniform with exponential refinement near the electrode and membrane interfaces. A standard projection method is used to ensure that the spatially interpolated velocity fields are divergence-free, such that they obey hydrodynamic mass conservation. Finally, since the time step  $\Delta t = 2 \times 10^{-3} \text{ s}$  is smaller than the interval between velocity field measurements, inter-measurement velocity fields are computed using linear interpolation.

Second-order central differences are used in space and a forward-Euler scheme is used to advance in time. The resulting concentration field is used to compute  $D^0(x) = -(\overline{u'_x c'})$ . Since the initial condition for  $c$  is a uniform concentration, early time results are subject to transient phenomena that may contaminate the eddy diffusivity. We found that 5 s is sufficient for transients to dissipate; only data from after this time are used to compute  $D^0(x)$ . The values of physical constants used in all simulations are shown in Table II.

The measured eddy diffusivity profiles are shown in Fig. 4, where each curve corresponds to a single experiment conducted at a fixed mean applied electric potential. The profiles have been normalized by the ambipolar diffusivity, demonstrating that electroconvection may effectively enhance transport by over an order of magnitude in comparison to the diffusion of an electroneutral salt. Larger  $\Delta\phi$  values are associated with further enhancements in effective transport. Additionally, the profiles are asymmetric, exhibiting a global maximum that is closer to the cation-selective membrane than the anode. The eddy diffusivity's dependence on  $\Delta\phi$  and its spatial asymmetry corroborate the findings of several prior studies demonstrating that stronger advection is present at larger applied electric potentials, and that vortical structures in the flow tend to be concentrated near the ion-selective membrane.

The intuitive connection between scalar mixing and the eddy diffusivity is seen through examination of the instantaneous salt concentration fields in Fig. 5. These are not the  $c$  fields computed via Eq. (15) as part of the MFM procedure. Rather, we show the unforced fields from simulation of a passive scalar [Eq. (10)] in order to exemplify the correspondence between the eddy diffusivity and the unaltered system for which the eddy diffusivity is measured.

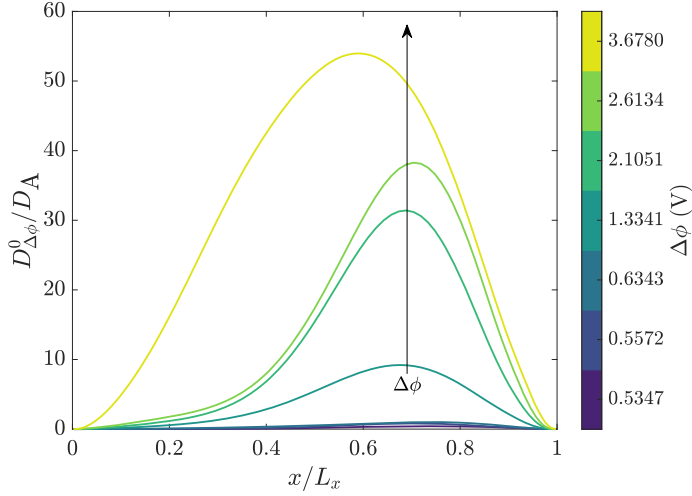


FIG. 4. Eddy diffusivity profiles for different applied potentials, normalized by the ambipolar diffusivity for copper sulfate. The subscript  $\Delta\phi$  in  $D_{\Delta\phi}^0(x)$  signifies that each profile is only valid for the specific  $\Delta\phi$  value corresponding to the experiment in which velocity fields were measured for that case.

Without electroconvection, the instantaneous salt concentration profiles are expected to be purely 1D, varying only in  $x$ . All cases shown in Fig. 5 contain variations in  $y$  (and in  $z$ , though not displayed here), which develop when the electrolyte is mixed by advection. Electroconvection first

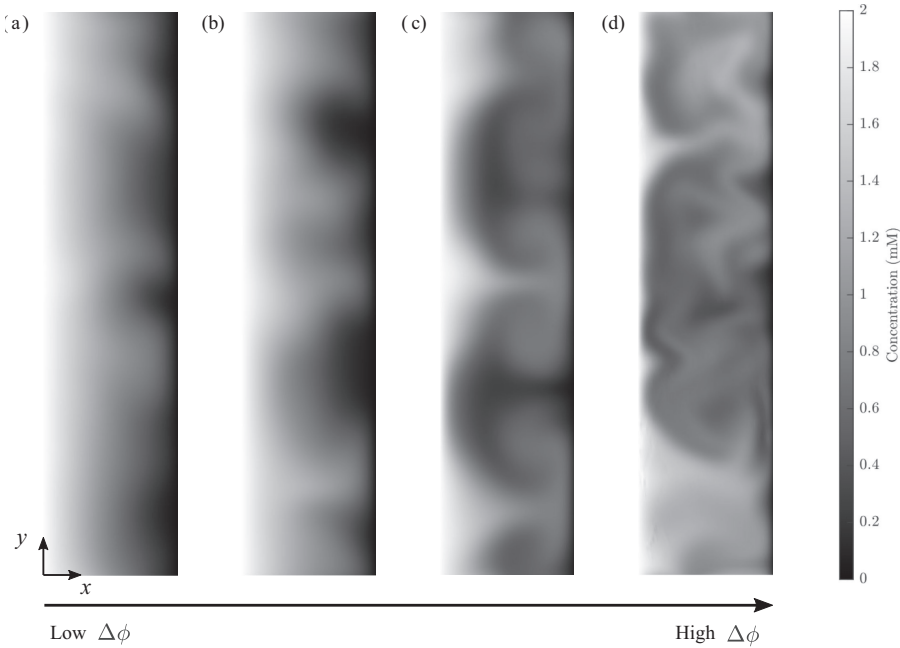


FIG. 5. Instantaneous salt concentration fields computed via Eq. (10) for (a)  $\Delta\phi = 0.5347$ , (b)  $\Delta\phi = 0.6343$ , (c)  $\Delta\phi = 2.1051$ , and (d)  $\Delta\phi = 3.6780$ . These are not the  $c$  fields computed via Eq. (15) as part of the MFM procedure. Rather, we show the unforced fields in order to develop an intuitive connection between the eddy diffusivity and the unaltered system for which the eddy diffusivity is measured.



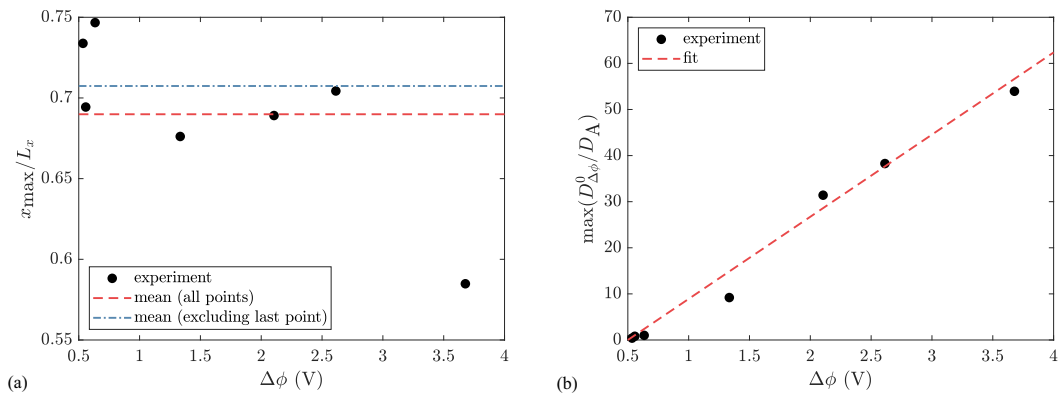


FIG. 6. Analysis of the shape and the magnitude of the eddy diffusivity profiles measured at different applied electric potentials. (a)  $x_{\max}$ , the location of the maximum value of  $D_{\Delta\phi}^0(x)$ . The mean is shown with and without the last point, since the diffusivity profile corresponding to that case is qualitatively different from the other cases due to the effects of confinement. (b) The maximum value of  $D_{\Delta\phi}^0(x)$  for different  $\Delta\phi$ . Also shown is a linear fit based on least-squares regression.

develops at the electrolyte-membrane interface, which occurs at the right side of each panel in Fig. 5. As  $\Delta\phi$  is increased, the perturbations in the concentration fields become stronger, extending further from the membrane. Figure 5(c) in particular exhibits mushroom-like structures, which are indicative of vortical flow penetrating deep into the electrolyte. Additionally, the higher  $\Delta\phi$  cases are associated with thinner features in the concentration fields, which are more prone to mixing via molecular diffusion. Thus, the enhancement in mixing captured by the eddy diffusivity may be attributed to both (i) the direct stirring of the electrolyte by velocity fields and (ii) the subsequent molecular diffusion of thin features that form when the electrolyte is stirred.

As structures in the velocity and concentration fields grow in size, they may be increasingly influenced by confinement due to the anode and its no-slip condition at the left side of the domain. This effect is seen in Fig. 5(d), the highest  $\Delta\phi$  case. The fine-scale structures in Fig. 5(d) signify a flow field that contains multiple vortices with varying sizes. However, the  $x$  extent of the domain is no longer large enough to contain the largest vortices that would be present were the equations solved in a semi-infinite domain. This offers an explanation for the qualitative difference between the eddy diffusivity for the largest  $\Delta\phi$  case and for the other profiles in Fig. 4.

We refer to the set of profiles shown in Fig. 4 as  $D_{\Delta\phi}^0(x)$ , where the subscript signifies that each profile is only valid at a specific  $\Delta\phi$  value corresponding to the experiment in which velocity fields were measured for that case. We now consider one approach to construct an eddy diffusivity profile that will be valid for intermediate values of applied electric potential. We refer to this second notion of eddy diffusivity as  $D^0(x, \Delta\phi)$ , signifying that it should be a continuous function of the applied electric potential. First, note that all the profiles shown in Fig. 4 contain a global maximum. We define  $x_{\max}$  as the location of this maximum value for each case. As shown in Fig. 6,  $x_{\max}$  does not vary significantly from case to case, with the exception of the largest  $\Delta\phi$ . We display the mean value of  $x_{\max}$  with and without the largest  $\Delta\phi$  case, since the largest case exhibits a significant qualitative difference from the other cases due to the effects of confinement. The maximum value of  $D_{\Delta\phi}^0(x)$  is shown in Fig. 6(b). In this work, we compute a linear fit using the least squares method, resulting in  $\max(D_{\Delta\phi}^0/D_A) = \alpha\Delta\phi + \gamma$  with  $\alpha = 17.82 \text{ V}^{-1}$  and  $\gamma = -9.87$ .

Note that the critical  $\Delta\phi_{\text{cr}}$  for onset of electroconvection occurs when  $\alpha\Delta\phi_{\text{cr}} + \gamma = 0$ , yielding  $\Delta\phi_{\text{cr}} = 0.55 \text{ V}$ . This prediction agrees well with prior experimental, theoretical, and computational predictions of the critical applied potential for the onset of electroconvection [26,40,45]. Furthermore, the linear form chosen here naturally guarantees that  $\max(D_{\Delta\phi}^0/D_A)$  is precisely zero for  $\Delta\phi = \Delta\phi_{\text{cr}}$  and positive for  $\Delta\phi > \Delta\phi_{\text{cr}}$ .

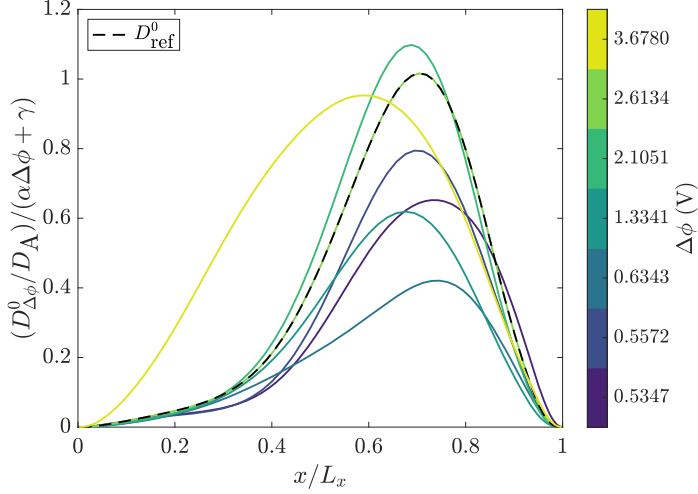


FIG. 7. Each of the  $D_{\Delta\phi}^0$  profiles has been scaled by  $\alpha\Delta\phi + \gamma$ , where  $\alpha$  and  $\gamma$  are found from a linear fit of the maximum of  $D_{\Delta\phi}^0$  as a function of  $\Delta\phi$ . We may construct a voltage–dependent form of the eddy diffusivity by selecting one of these profiles as the reference profile  $D_{\text{ref}}^0$ , indicated here as black dashed curve.

Based on the observations in Fig. 6, we construct a simple voltage–dependent form for the eddy diffusivity. We begin by attempting to collapse the diffusivity profiles for different applied electric potentials. In Fig. 7, we display the results of scaling each diffusivity profile by  $\alpha\Delta\phi + \gamma$ . The qualitative similarity of the different profiles and tight variation in  $x_{\text{max}}$  (for all cases except the largest applied potential) suggest that we may model the scaled diffusivity profiles using a common reference profile. In this work, we simply select  $D_{\Delta\phi}^0/(\alpha\Delta\phi + \gamma)$  for the case of  $\Delta\phi = 2.6134$  V as the reference profile (shown as a dashed black line in Fig. 7, denoted  $D_{\text{ref}}^0$ ). Note that in Fig. 6(a), the shape of the profile for this case is such that the location of the maximum ( $x_{\text{max}}$ ) falls closest to the average for all cases excluding the largest  $\Delta\phi$ .

Thus, we can write an eddy diffusivity with analytically prescribed dependence on  $\Delta\phi$  that is valid for all overlimiting applied potential values. We write

$$D^0(x, \Delta\phi) = (\alpha\Delta\phi + \gamma)D_{\text{ref}}^0(x), \quad (20)$$

which is valid for  $\Delta\phi \geq \Delta\phi_{\text{cr}}$ . No supplementary eddy diffusivity is required for underlimiting and limiting applied electric potentials (i.e.,  $\Delta\phi < \Delta\phi_{\text{cr}}$ ).

### B. One-dimensional simulations with eddy diffusivity

Finally, we present a realistic, “*a posteriori*” evaluation of how well the measured 1D eddy diffusivity profiles capture the macroscopic transport effects of chaotic, 3D electroconvection and thereby enable accurate prediction of system performance without expensive 3D DNS. We begin by recapitulating the macroscopic ion transport equations, which we present here in their fully closed form:

$$\frac{\partial \bar{c}_i}{\partial t} = \frac{\partial}{\partial x} \left\{ [D_i + D^0(x)] \frac{\partial \bar{c}_i}{\partial x} + D_i \frac{z_i e}{k_B T} \bar{c}_i \frac{\partial \bar{\phi}}{\partial x} \right\} \quad (21)$$

and

$$-\varepsilon_0 \varepsilon_r \frac{\partial^2 \bar{\phi}}{\partial x^2} = \sum_i e z_i \bar{c}_i. \quad (22)$$

Equations (21) and (22) are simply the Reynolds-averaged Poisson-Nernst-Planck equations, in which the advective closure flux is modeled using  $D^0$ . We concluded the previous section with two versions of the eddy diffusivity:  $D_{\Delta\phi}^0(x)$  is measured exactly at each corresponding  $\Delta\phi$  value that was applied in the experiment, while  $D^0(x, \Delta\phi)$  is a fitted profile. We assess the performance of each option in turn. Regardless of which form of the eddy diffusivity is used in place of  $D^0(x)$  in Eq. (21), the additional cost of including  $D^0(x)$  in Eqs. (21) and (22) is negligible, allowing time-to-solution of seconds or minutes on desktop computers.

We now describe the boundary conditions and initial condition for Eqs. (21) and (22). An electrode is present at  $x = 0$ , where the no-flux condition is applied for  $\text{SO}_4^{2-}$  and a Dirichlet condition is applied for  $\text{Cu}^{2+}$ . Meanwhile, the electric potential at the electrode is assigned a reference value of zero:

$$\left\{ -[D_i + D^0(x)] \frac{\partial \bar{c}_i}{\partial x} - D_i \frac{z_i e}{k_B T} \bar{c}_i \frac{\partial \bar{\phi}}{\partial x} \right\} \Big|_{x=0} = 0 \quad \text{for } i = \text{SO}_4^{2-}, \quad (23a)$$

$$\bar{c}_i(x=0) = c_E \quad \text{for } i = \text{Cu}^{2+}, \quad (23b)$$

$$\bar{\phi}(x=0) = 0. \quad (23c)$$

We use a value of  $c_E = 1 \text{ mmolL}^{-1}$  in Eq. (23). An electric double layer is expected to form at the electrode, in which  $\text{SO}_4^{2-}$  ions accumulate and  $\text{Cu}^{2+}$  ions are depleted. Though the choice of  $c_E$  affects the concentration profiles inside this EDL, we have confirmed that concentration and electric potential profiles outside of the EDL are not affected by the specific choice of  $c_E$ , as long as  $c_E$  is smaller than the  $\text{Cu}^{2+}$  concentration just outside the EDL. Examination of Fig. 8(a) permits after-the-fact confirmation that our choice of  $c_E = 1 \text{ mmolL}^{-1}$  satisfies this condition. Additionally, we have confirmed that the influence of variation in  $c_E$  on the current-voltage curve is negligible: changing  $c_E$  by an order of magnitude leads to 0.2% variation in the simulated current density.

The cation-selective membrane is present at  $x = L_x$ . A no-flux condition is applied to  $\text{SO}_4^{2-}$  ions, representing perfect co-ion exclusion. Meanwhile, a Dirichlet condition is applied for  $\text{Cu}^{2+}$  ions and for the electric potential:

$$\left\{ -[D_i + D^0(x)] \frac{\partial \bar{c}_i}{\partial x} - D_i \frac{z_i e}{k_B T} \bar{c}_i \frac{\partial \bar{\phi}}{\partial x} \right\} \Big|_{x=L_x} = 0 \quad \text{for } i = \text{SO}_4^{2-}, \quad (24a)$$

$$\bar{c}_i(x=L_x) = c_M \quad \text{for } i = \text{Cu}^{2+}, \quad (24b)$$

$$\bar{\phi}(x=L_x) = -\Delta\phi. \quad (24c)$$

The boundary conditions in Eq. (24) are asymptotically valid for a cation-selective membrane, provided  $c_M$  is larger than the bulk electrolyte concentration [26]. Dependence on  $c_M$  has been shown to be practically nonexistent in prior high-fidelity simulations [44]. In this work, we select a value of  $c_M = 2 \text{ mmolL}^{-1}$ .

At  $t = 0$  in all simulations, the ion concentration throughout the domain is fixed at

$$\bar{c}_i(t=0) = 1 \text{ mmolL}^{-3}, \quad (25)$$

and the electric potential is taken to have a linear profile between the boundary condition values. The simulation is time-advanced until steady state, and the values of all physical constants used in these simulations can be found in Table II. We use second-order central differences in space and a second-order implicit scheme in time [45].

We begin by examining results obtained using the measured  $D_{\Delta\phi}^0$  profiles. The resulting mean concentration and electric potential profiles are shown in Fig. 8. Mean  $\text{Cu}^{2+}$  concentration is shown as a solid line, while mean  $\text{SO}_4^{2-}$  concentration is shown as a dashed line. In Fig. 8(a), a linear profile is seen for lower applied potentials, and an inflection point develops as applied potential is increased and electroconvection becomes stronger. On average, electroconvection helps transport

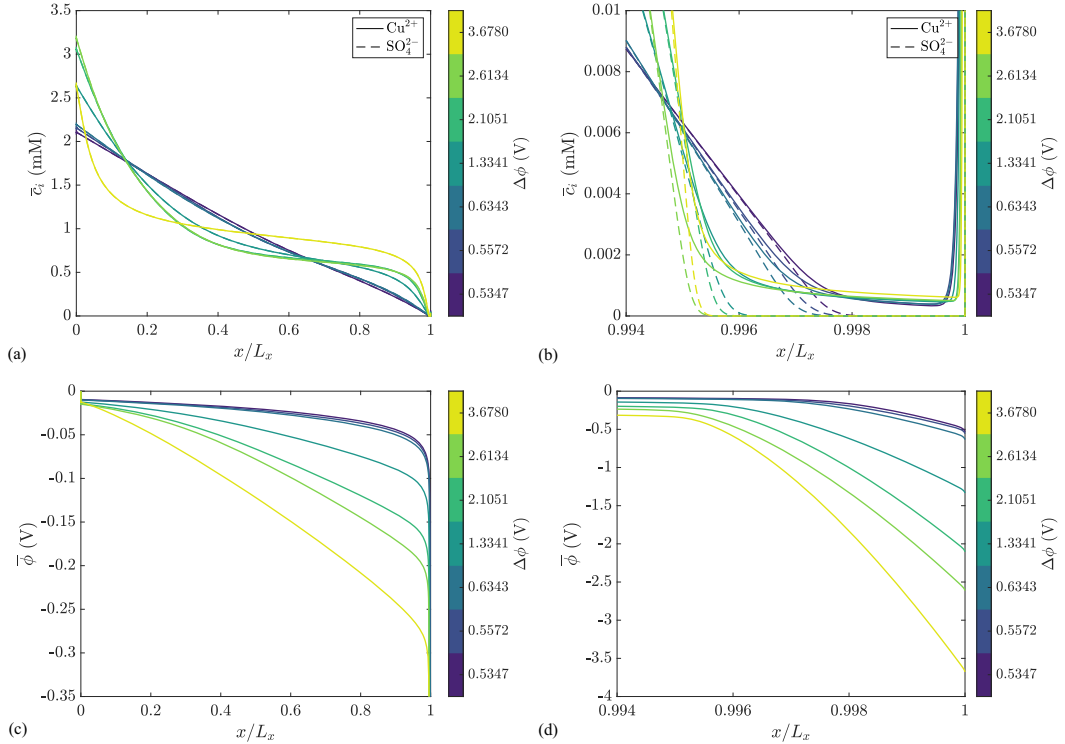


FIG. 8. Mean concentration and electric potential profiles computed directly from the closed macroscopic equations using  $D_{\Delta\phi}^0$ . Mean  $\text{Cu}^{2+}$  concentration is shown as a solid line, while mean  $\text{SO}_4^{2-}$  concentration is shown as a dashed line. Electric potential is shown as a solid line. (a) A view of the entire domain. Due to electroneutrality throughout most of the domain, the two species' concentration curves are indistinguishable. (b) A zoomed-in view of the near-membrane region, highlighting the double layer and extended space charge regions. (c) Electric potential, over the entire domain. (d) Electric potential in the near-membrane region.

ions from the electrode toward the membrane, as evidenced by the enhanced ion concentration on the right side of the domain and reduced concentrations on the left for larger values of  $\Delta\phi$ . The cation and anion curves are visibly indistinguishable in panel (a), since the electrolyte is largely electroneutral outside of the thin double layers. We do, indeed, resolve the EDLs, as shown in Fig. 8(b). Furthermore, an ESC region is clearly visible here for all cases. The mean electric potential profiles are shown in Figs. 8(c) and 8(d), demonstrating that a significant portion of the potential drop occurs in the near-membrane region—in the ESC and EDL layers specifically, which suffer from lower conductivity due to relative ion depletion.

We now wish to determine the extent to which the features described above are a direct consequence of the measured eddy diffusivity profiles. In Fig. 9(a), we solve the macroscopic equations [Eqs. (21) and (22)] without including any kind of eddy diffusivity (i.e., by setting  $D^0 = 0$ ), to demonstrate the consequences of neglecting the unclosed fluxes entirely. In the absence of any representation of mixing due to electroconvection, the concentration profiles remain linear in the electroneutral bulk. This behavior is expected based on analysis of Eqs. (21) and (22) in the limit of quasielectroneutrality, where the method of matched asymptotic expansions may be used to determine an “outer solution” that is valid outside of the EDL and ESC zones [24]. The contrast between Figs. 9(a) and 8(a) demonstrates that inclusion of the eddy diffusivity plays a dominant role in the system's dynamics.

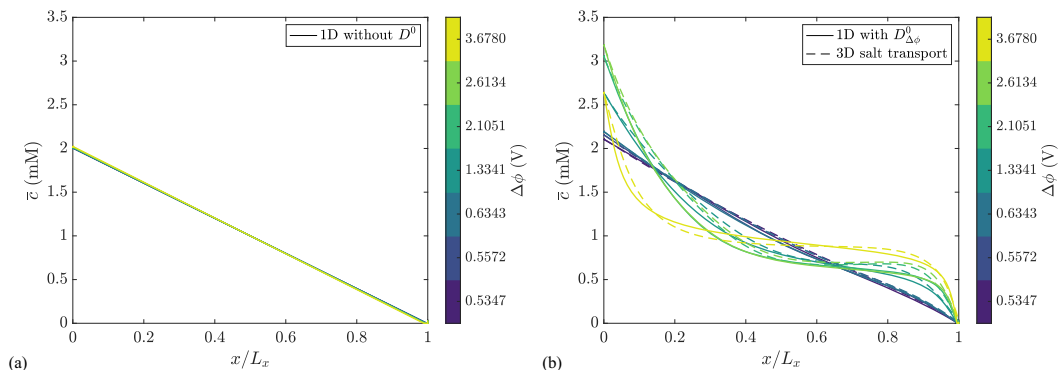


FIG. 9. (a) Mean electroneutral salt concentration computed using the standard 1D Poisson–Nernst–Planck equations in the absence of  $D^0$ . Without the representation of mixing due to microscopic vortices, the profiles remain linear. (b) Mean electroneutral salt concentration computed via two different methods. The direct 1D simulations of Eqs. (21) and (22) using  $D^0_{\Delta\phi}$  are shown as solid curves. The dashed curves are computed via  $y$ ,  $z$ , and  $t$  averaging applied to the fields resulting from 3D simulation of Eq. (10), in which the measured velocity fields mix the electroneutral salt. Quantitative agreement demonstrates that the leading order eddy diffusivity is capable of capturing the macroscopic transport effects of electroconvection.

To assess how accurately the eddy diffusivity serves as a macroscopic representation of microscopic mixing, we may directly compare the mean profiles generated via the macroscopic and microscopic routes. In Fig. 9(b), the mean profiles computed directly by solving the macroscopic equations using  $D^0_{\Delta\phi}$  are shown as solid curves. Alternatively, we may compute the mean profiles by first solving an equation for instantaneous 3D (microscopic) transport of an electroneutral salt via Eq. (10) (as was performed to show the concentration profiles in Fig. 5) and then performing averages in  $y$ ,  $z$ , and  $t$ . The results of the latter approach are shown as dashed curves in Fig. 9(b), exhibiting good agreement with the directly computed 1D results. Discrepancies between the two approaches can be attributed to the fact that we have only retained the leading order term in Eq. (13) for our eddy diffusivity model. As seen, however, the leading order term alone is sufficient to provide accurate mean concentration profiles across a wide range of applied electric potential in the overlimiting regime.

Starting from the macroscopic ionic concentration and electric potential profiles shown in Fig. 8, we may build a more detailed understanding of transport by examining the influence of the flux terms in Eq. (21), the macroscopic species transport equation. Each term is plotted in a panel of Fig. 10, where a positive flux corresponds to transport in the positive  $x$  direction (i.e., aligned with the electric field). We have verified that a summation of the individual flux terms yields a constant total flux across the entire domain for the cation and zero total flux across the entire domain for the anion, as expected at equilibrium for every case given the boundary conditions in Eqs. (23) and (24).

At low applied electric potentials, the advective closure flux is negligible while the diffusion and electromigration fluxes are dominant and of similar order to each other. The two dominant fluxes sum together to produce a finite flux for cations, while they cancel out to produce zero-flux for the anions (due to a sign difference in the electromigration term between the cation and the anion). At high applied electric potentials, the diffusion flux is negligible compared to the advective closure and electromigration fluxes, providing additional evidence that the advective closure plays a dominant role in the macroscopic physics. The interaction of the dominant fluxes is similar to the previously described case: the dominant fluxes sum to a finite flux for cations and zero-flux for anions.

Next, we compute the mean current density for each  $D^0_{\Delta\phi}$  and compare the resulting  $j$ -V curve against that measured in experiments. Since Fig. 10 indicates that all current is carried by cations,

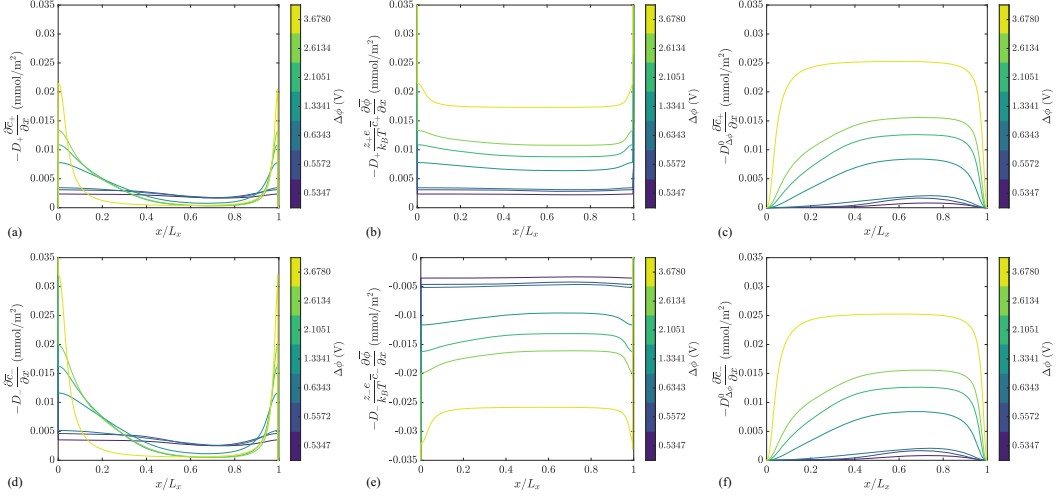


FIG. 10. Contributions of individual terms to the overall ionic flux in the electroneutral bulk region. Panels (a–c) are the diffusion flux, electromigration flux, and advective closure flux, respectively, for  $\text{Cu}^{2+}$ . Panels (d–f) are the diffusion flux, electromigration flux, and advective closure flux, respectively, for  $\text{SO}_4^{2-}$ . Electromigration and diffusion are the dominant terms throughout most of the electroneutral bulk region at lower applied electric potentials, while electromigration and the advective closure flux are the dominant terms at higher applied electric potentials.

we may write the current density as

$$j = z_+ e F \left\{ -[D_+ + D^0(x)] \frac{\partial \bar{c}_+}{\partial x} - D_i \frac{z_+ e}{k_B T} \bar{c}_+ \frac{\partial \bar{\phi}}{\partial x} \right\}, \quad (26)$$

which may be evaluated at any point in space since the total flux is constant.  $F$  is Faraday's constant. The result is shown in Fig. 11(a). The standard 1D Poisson–Nernst–Planck equations (dash-dot red

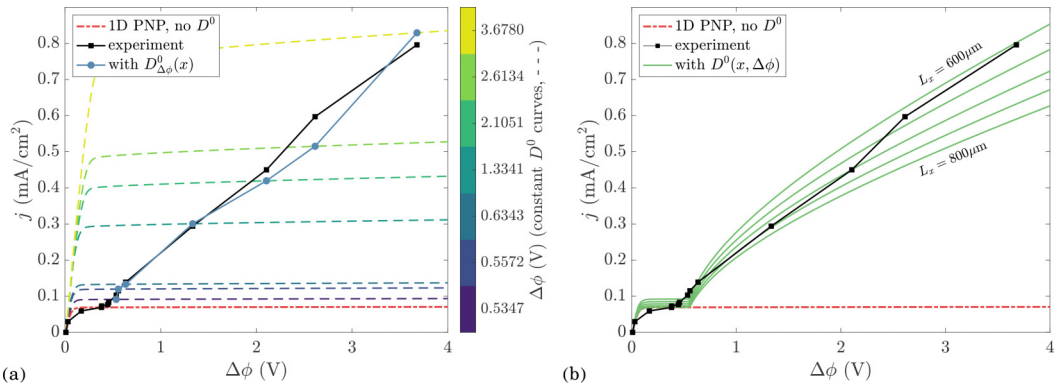


FIG. 11. Mean current-voltage curves produced using the eddy diffusivity. In both panels, results of the standard 1D Poisson–Nernst–Planck equations are shown as dash-dot red curves, and the experiment points are shown using black squares. (a) The current density computed using each of the directly measured diffusivity profiles  $D_{\Delta\phi}^0$  is shown as a blue circle. The dashed curves correspond to j–V sweeps in which the same eddy diffusivity profile was used for the entire range of applied electric potentials. (b) The j–V curves computed using the  $\Delta\phi$ -dependent diffusivity profiles,  $D^0(x, \Delta\phi)$ , for a range of  $L_x$  values.



curve) compare well to experiments (solid black curve) in the under-limiting and limiting regimes. As soon as electroconvection begins, however, utilization of the eddy diffusivity is necessary and produces remarkable quantitative agreement with the experiments (solid blue curve versus solid black curve).

The dashed curves in Fig. 11(a) are j-V sweeps that were performed with a fixed  $D_{\Delta\phi}^0$  profile throughout each sweep, corresponding to the  $\Delta\phi$  shown in the colorbar. The dashed curves reveal a broad limiting region for each eddy diffusivity profile, over which variation in applied voltage leads to small changes in the measured current. Therefore, errors in the potential-correction procedure described in Sec. III are not expected to significantly alter the results. Modification of parameters like  $\beta$ ,  $i_0$ , or  $\rho_{\text{bulk}}L_{\text{bulk}}$  will in turn modify the  $\Delta\phi$  that must be used in *a posteriori* simulations, but changes in  $\Delta\phi$  ultimately lead to minimal changes in the measured current density.

Finally, we demonstrate usage of the semianalytically fitted  $\Delta\phi$ -dependent diffusivity profile given by  $D^0(x, \Delta\phi)$  in Eq. (20). Since the mean concentration and electric potential profiles computed using  $D^0(x, \Delta\phi)$  are qualitatively very similar to those shown in Fig. 8, we reserve discussion of the mean profiles for the Appendix. Instead, we will proceed directly to discussion of j-V curves that are produced using this form of the eddy diffusivity.

The main benefit of using  $D^0(x, \Delta\phi)$  in place of  $D_{\Delta\phi}^0$  is the ability to produce j-V curves that are smooth functions of the applied electric potential. However, comparison with the experiments (which were conducted at discrete values of the applied electric potential) is complicated by the presence of experimental errors: since the parameter  $L_x$  varies from case to case due to imprecision in the experimental setup, the value of  $L_x$  for intermediate applied potentials is not well defined. To allow a reasonable comparison, we consider a range of  $L_x$  values between 600  $\mu\text{m}$  and 800  $\mu\text{m}$ . One j-V curve is produced for each choice of  $L_x$ , as shown in Fig. 11(b), exhibiting good agreement between the model and experiments. The j-V curves produced using  $D^0(x, \Delta\phi)$  exhibit a noticeable downward-concavity for all choices of  $L_x$ , particularly for low-overlimiting applied potentials. The curves gradually approach linear behavior at larger  $\Delta\phi$  values. This result is qualitatively similar to Druzgalski and coauthors' DNS of chaotic electroconvection [45], though quantitative agreement is prohibited by differences in the values of nondimensional parameters between the two works (particularly since the ions in this work are divalent).

## V. DISCUSSION AND CONCLUSION

The motivation for this work lay in the observation that mean concentration and electric potential fields are sufficient to determine the power usage and ion exchange rate for the practical design of systems that exhibit electroconvection, despite the presence of chaotic spatiotemporal fluctuations at much smaller scales. We utilized this observation as the guiding principle for our model reduction approach, but the application of Reynolds-averaging to the microscopic equations leads to a closure problem that must be addressed before the macroscopic system can be solved. The MFM procedure allowed us to develop a leading order representation of the dominant unclosed flux, revealing a simple gradient-diffusion operator. Furthermore, we measured the corresponding eddy diffusivity from experiments by inserting experimental velocity fields into the MFM procedure, circumventing the need for prohibitively expensive DNS-derived velocity fields. We found that 1D simulations using the measured eddy diffusivity produce current-voltage curves that agree quantitatively with experiments.

There are three limitations of this work that are worth briefly discussing. First, the utilization of averaging as an avenue for model-reduction leads to strong dependence on the geometry of the cell in which electroconvection occurs. For example, in a simple planar geometry operating in a stationary state, a 1D and steady representation is wholly appropriate. However, membrane heterogeneity in the  $y$  and  $z$  directions (an area of recent interest [49–52,62]) would complicate the reduction of those dimensions. Consider the worst-case scenario, in which some electrochemical system lacks homogeneity in all three spatial dimensions and is operating in an unsteady (i.e., pulsed, for example) fashion. In this case, only ensemble averaging may be performed. Though

the number of dimensions has not been reduced, the solution may be represented more coarsely in time and space since ensemble averaging will still eliminate fine-scale structures. Ultimately, however, the eddy diffusivity computed using our method is still geometrically contingent on the original problem setup. Future researchers who seek to develop a stand-alone reduced-order model for electroconvection may use our diffusivity profiles as a benchmark for their work.

Second, though there were two unclosed terms in Eq. (8), we only developed a closure model for the dominant term while neglecting the other. Our results indicate that this approach is sufficient to achieve quantitative agreement with the experiments. Nonetheless, the determination of a closure model for the lesser of the unclosed terms in Eq. (8) may be worthy of additional consideration in some circumstances. As was the case for the error induced by working with the electroneutral salt transport equation instead of individual ionic transport equations, we expect the error due to neglecting the second unclosed term to be dependent on the Debye length. As such, these effects may become important in situations where the double layers are relatively thick and regions featuring strong advection also exhibit appreciable nonelectroneutrality.

Third, recall that the utilization of experimental velocity fields is central to this work. Though the incorporation of experimental data into a largely computational technique allowed us to bypass expensive DNS of the full Poisson–Nernst–Planck–Stokes equations, the purely computational approach would be free of the sources of error in experiments—e.g., variation of the domain size from case to case and deformation of the membrane during each experiment. Thus, a purely computational approach may allow for a more precise determination of the correct reference diffusivity profile  $D_{\text{ref}}^0$  for use in  $D^0(x, \Delta\phi)$ . Additionally, while we have used a simple linear fit to describe how the magnitude of the eddy diffusivity varies with the applied electric potential, performing the purely computational MFM procedure for a large number of  $\Delta\phi$  values may reveal a more complicated relationship.

The physical insight demonstrated in this work—namely, a quantitative demonstration that the macroscopic effects of microscopic mixing may be represented as an effective diffusion process—brings new insight to the study of electroconvection, since such an approach has not been used before to develop a reduced-order model in this field. We’ve also demonstrated a methodological innovation, wherein components of a chiefly computational procedure were replaced with data from experiments, allowing us to directly measure the closure operator associated with experimental velocity fields. Such a technique may be applied to other geometries in which electroconvection occurs, and to problems other than electroconvection, in which a macroscopic representation of mixing due to chaotic, fine-scale velocity fields is desired.

#### ACKNOWLEDGMENTS

This work was supported by the National Science Foundation under Grant No. 1553275, and the Office of Naval Research. A.B. was additionally supported by the C. H. Kruger Stanford Graduate Fellowship. F.S. was supported by a Fulbright Fellowship. The one-dimensional simulation code utilized in this work was developed with support from the Solar Photochemistry and Catalysis Programs of the Chemical Sciences, Geosciences, and Biosciences Division, Office of Basic Energy Sciences, U.S. Department of Energy, under Grant No. DE-SC0021633.

#### APPENDIX: MACROSCOPIC CONCENTRATION AND ELECTRIC POTENTIAL PROFILES COMPUTED USING $D^0(x, \Delta\phi)$

In this Appendix, we briefly discuss the macroscopic concentration and electric potential profiles shown in Fig. 12, which are computed using  $D^0(x, \Delta\phi)$ . Profiles are displayed for each applied electric potential value that was probed in the experiments. The value of  $L_x$  used for each simulation matches the value measured in experiments, as shown in Table I. Generally, we observe qualitative similarity to the results shown in Fig. 8, which were computed using  $D_{\Delta\phi}^0$ . Closer examination reveals quantitative differences, particularly for the largest value of applied electric potential.

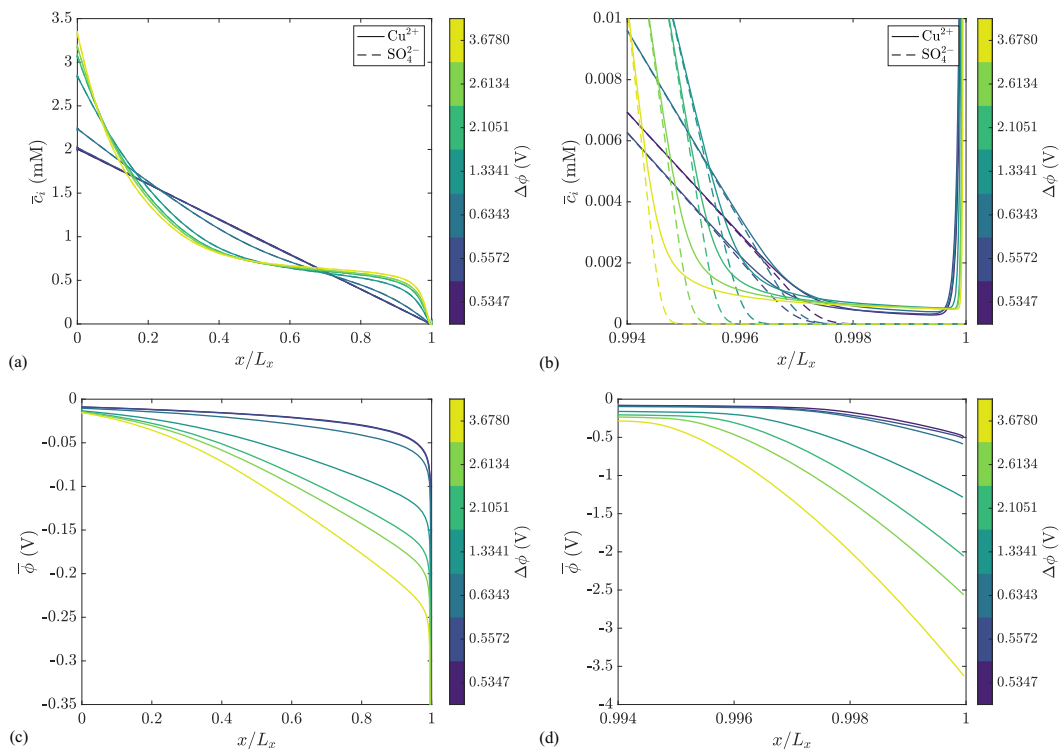


FIG. 12. Mean concentration and electric potential profiles computed directly from the closed macroscopic equations using  $D^0(x, \Delta\phi)$ . Mean  $\text{Cu}^{2+}$  concentration is shown as a solid line, while mean  $\text{SO}_4^{2-}$  concentration is shown as a dashed line. Electric potential is shown as a solid line. (a) A view of the entire domain. Due to electroneutrality throughout most of the domain, the two species' concentration curves are indistinguishable. (b) A zoomed-in view of the near-membrane region, highlighting the double layer and extended space charge regions. (c) Electric potential, over the entire domain. (d) Electric potential in the near-membrane region.

Recall that the diffusivity profile measured for the case of  $\Delta\phi = 3.6780$  V bears significant qualitative differences compared to the other cases, as is evident from Figs. 4, 6, and 7. Though the maximum value generally follows the linear trend with respect to  $\Delta\phi$ , the location of the maximum value is much closer to the center of the domain than in all the other cases. Examination of Fig. 5 revealed that this case is affected by confinement, since vortical structures in the flow have grown large enough to interact with the no-slip electrode at  $x = 0$ .

Because of the way  $D^0(x, \Delta\phi)$  is computed [linear extrapolation in  $\Delta\phi$  starting at an intermediate value, as shown in Eq. (20)], the profile given by  $D^0(x, \Delta\phi = 3.6780$  V) is not affected by confinement—its shape remains similar to that of the other profiles, with a maximum value that is located closer to the membrane than to the electrode. Furthermore, as a result of the  $\Delta\phi$ -dependent eddy diffusivity's smooth and monotonic variation in  $\Delta\phi$ , the macroscopic concentration profiles computed using  $D^0(x, \Delta\phi)$  also exhibit smooth, monotonic variation with respect to  $\Delta\phi$ . This can be seen by comparing Figs. 8(a) and 8(b) to Figs. 12(a) and 12(b), specifically examining the concentration profile for the largest applied electric potential.

We note, however, that results generated using  $D^0(x, \Delta\phi)$  may not be accurate for the largest value of  $\Delta\phi$ , precisely because they do not account for confinement. Confinement is expected to occur and must be accounted for once coherent structures associated with the velocity field are large enough to interact with the no-slip boundary condition at the electrode. The large qualitative difference in the measured diffusivity profile for the largest applied electric potential is the measured

effect of confinement at the electrode, which leads to a differently shaped diffusivity profile and invalidates usage of  $D^0(x, \Delta\phi)$ . For intermediate  $\Delta\phi$  values, however,  $D^0(x, \Delta\phi)$  is still expected to produce accurate results.

---

- [1] H. Strathmann, Electrodialysis, a mature technology with a multitude of new applications, [Desalination](#) **264**, 268 (2010).
- [2] A. Campione, L. Gurreri, M. Ciofalo, G. Micale, A. Tamburini, and A. Cipollina, Electrodialysis for water desalination: A critical assessment of recent developments on process fundamentals, models and applications, [Desalination](#) **434**, 121 (2018).
- [3] L. Gurreri, A. Tamburini, A. Cipollina, and G. Micale, Electrodialysis applications in wastewater treatment for environmental protection and resources recovery: A systematic review on progress and perspectives, [Membranes](#) **10**, 146 (2020).
- [4] T. Xu and C. Huang, Electrodialysis-based separation technologies: A critical review, [AIChE J.](#) **54**, 3147 (2008).
- [5] M. Fidaleo and M. Moresi, Electrodialysis applications in the food industry, [Adv. Food Nutr. Res.](#) **51**, 265 (2006).
- [6] V. Fleury, J. N. Chazalviel, and M. Rosso, Coupling of drift, diffusion, and electroconvection, in the vicinity of growing electrodeposits, [Phys. Rev. E](#) **48**, 1279 (1993).
- [7] J. M. Huth, H. L. Swinney, W. D. McCormick, A. Kuhn, and F. Argoul, Role of convection in thin-layer electrodeposition, [Phys. Rev. E](#) **51**, 3444 (1995).
- [8] J. Tan and E. M. Ryan, Computational study of electro-convection effects on dendrite growth in batteries, [J. Power Sources](#) **323**, 67 (2016).
- [9] G. Li, L. A. Archer, and D. L. Koch, Electroconvection in a viscoelastic electrolyte, [Phys. Rev. Lett.](#) **122**, 124501 (2019).
- [10] D. Zhang, A. J. Warren, G. Li, Z. Cheng, X. Han, Q. Zhao, X. Liu, Y. Deng, and L. A. Archer, Electrodeposition of zinc in aqueous electrolytes containing high molecular weight polymers, [Macromolecules](#) **53**, 2694 (2020).
- [11] M. C. Ma, G. Li, X. Chen, L. A. Archer, and J. Wan, Suppression of dendrite growth by cross-flow in microfluidics, [Sci. Adv.](#) **7**, eabf6941 (2021).
- [12] J. R. Melcher and G. I. Taylor, Electrohydrodynamics: A review of the role of interfacial shear stresses, [Annu. Rev. Fluid Mech.](#) **1**, 111 (1969).
- [13] D. A. Saville, Electrohydrodynamics: The Taylor-Melcher leaky dielectric model, [Annu. Rev. Fluid Mech.](#) **29**, 27 (1997).
- [14] O. Schnitzer and E. Yariv, The Taylor-Melcher leaky dielectric model as a macroscale electrokinetic description, [J. Fluid Mech.](#) **773**, 1 (2015).
- [15] M. Z. Bazant, Electrokinetics meets electrohydrodynamics, [J. Fluid Mech.](#) **782**, 1 (2015).
- [16] I. Rubinstein and L. Shtilman, Voltage against current curves of cation exchange membranes, [J. Chem. Soc., Faraday Trans. 2](#) **75**, 231 (1979).
- [17] F. Maletzki, H. W. Rösler, and E. Staude, Ion transfer across electrodialysis membranes in the overlimiting current range: stationary voltage current characteristics and current noise power spectra under different conditions of free convection, [J. Membr. Sci.](#) **71**, 105 (1992).
- [18] I. Rubinstein, Electroconvection at an electrically inhomogeneous permselective interface, [Phys. Fluids A](#) **3**, 2301 (1991).
- [19] I. Rubinstein and F. Maletzki, Electroconvection at an electrically inhomogeneous permselective membrane surface, [J. Chem. Soc., Faraday Trans.](#) **87**, 2079 (1991).
- [20] A. Mani and K. M. Wang, Electroconvection near electrochemical interfaces: Experiments, modeling, and computation, [Annu. Rev. Fluid Mech.](#) **52**, 509 (2020).
- [21] V. V. Nikonenko, S. Mareev, N. D. Pismenskaya, A. M. Uzdanova, A. V. Kovalenko, M. K. Urtenov, and G. Pourcelly, Effect of electroconvection and its use in intensifying the mass transfer in electrodialysis (Review), [Russ. J. Electrochem.](#) **53**, 1122 (2017).

- [22] V. V. Nikonenko, V. I. Vasil'eva, E. M. Akberova, A. M. Uzdenova, M. K. Urtenov, A. V. Kovalenko, N. P. Pismenskaya, S. Mareev, and G. Pourcelly, Competition between diffusion and electroconvection at an ion-selective surface in intensive current regimes, *Adv. Colloid Interface Sci.* **235**, 233 (2016).
- [23] V. V. Nikonenko, A. V. Kovalenko, M. K. Urtenov, N. D. Pismenskaya, J. Han, P. Sizat, and G. Pourcelly, Desalination at overlimiting currents: State-of-the-art and perspectives, *Desalination* **342**, 85 (2014).
- [24] I. Rubinstein and B. Zaltzman, Electro-osmotically induced convection at a permselective membrane, *Phys. Rev. E* **62**, 2238 (2000).
- [25] I. Rubinstein and B. Zaltzman, Electro-osmotic slip of the second kind and instability in concentration polarization at electrodialysis membranes, *Math. Models Methods Appl. Sci.* **11**, 263 (2001).
- [26] B. Zaltzman and I. Rubinstein, Electro-osmotic slip and electroconvective instability, *J. Fluid Mech.* **579**, 173 (2007).
- [27] W. H. Smyrl and J. Newman, Double layer structure at the limiting current, *Trans. Faraday Soc.* **63**, 207 (1967).
- [28] S. S. Dukhin, Electrokinetic phenomena of the second kind and their applications, *Adv. Colloid Interface Sci.* **35**, 173 (1991).
- [29] S. S. Dukhin and N. A. Mishchuk, Intensification of electrodialysis based on electroosmosis of the second kind, *J. Membr. Sci.* **79**, 199 (1993).
- [30] E. K. Zholkovskij, M. A. Vorotyntsev, and E. Staude, Electrokinetic instability of solution in a plane-parallel electrochemical cell, *J. Colloid Interface Sci.* **181**, 28 (1996).
- [31] S. M. Rubinstein, G. Manukyan, A. Staicu, I. Rubinstein, B. Zaltzman, R. G. H. Lammertink, F. Mugele, and M. Wessling, Direct observation of a nonequilibrium electro-osmotic instability, *Phys. Rev. Lett.* **101**, 236101 (2008).
- [32] R. Kwak, G. Guan, W. K. Peng, and J. Han, Microscale electrodialysis: Concentration profiling and vortex visualization, *Desalination* **308**, 138 (2013).
- [33] R. Kwak, V. S. Pham, K. M. Lim, and J. Han, Shear flow of an electrically charged fluid by ion concentration polarization: Scaling laws for electroconvective vortices, *Phys. Rev. Lett.* **110**, 114501 (2013).
- [34] J. C. deValença, R. M. Wagterveld, R. G. H. Lammertink, and P. A. Tsai, Dynamics of microvortices induced by ion concentration polarization, *Phys. Rev. E* **92**, 031003(R) (2015).
- [35] S. V. Pham, H. Kwon, B. Kim, J. K. White, G. Lim, and J. Han, Helical vortex formation in three-dimensional electrochemical systems with ion-selective membranes, *Phys. Rev. E* **93**, 033114 (2016).
- [36] S. Kang and R. Kwak, Pattern formation of three-dimensional electroconvection on a charge selective surface, *Phys. Rev. Lett.* **124**, 154502 (2020).
- [37] B. Kim, S. Choi, V. S. Pham, R. Kwak, and J. Han, Energy efficiency enhancement of electromembrane desalination systems by local flow redistribution optimized for the asymmetry of cation/anion diffusivity, *J. Membr. Sci.* **524**, 280 (2017).
- [38] F. Stockmeier, L. Stüwe, C. Knepeck, S. Musholt, K. Albert, J. Linkhorst, and M. Wessling, On the interaction of electroconvection at a membrane interface with the bulk flow in a spacer-filled feed channel, *J. Membr. Sci.* **678**, 121589 (2023).
- [39] A. J. Warren, A. Sharma, D. Zhang, G. Li, and L. A. Archer, Structure and dynamics of electric-field-driven convective flows at the interface between liquid electrolytes and ion-selective membranes, *Langmuir* **37**, 5895 (2021).
- [40] F. Stockmeier, M. Schatz, M. Habermann, J. Linkhorst, A. Mani, and M. Wessling, Direct 3D observation and unraveling of electroconvection phenomena during concentration polarization at ion-exchange membranes, *J. Membr. Sci.* **640**, 119846 (2021).
- [41] F. Stockmeier, M. Schatz, M. Habermann, J. Linkhorst, A. Mani, and M. Wessling, Measurement of Electrokinetically induced hydrodynamics at Ion-selective interfaces using 3D Micro particle tracking velocimetry ( $\mu$ PTV), *MethodsX* **9**, 101814 (2022).
- [42] E. A. Demekhin, V. S. Shelistov, and S. V. Polyanskikh, Linear and nonlinear evolution and diffusion layer selection in electrokinetic instability, *Phys. Rev. E* **84**, 036318 (2011).

- [43] V. S. Pham, Z. Li, K. M. Lim, J. K. White, and J. Han, Direct numerical simulation of electroconvective instability and hysteretic current-voltage response of a permselective membrane, *Phys. Rev. E* **86**, 046310 (2012).
- [44] E. A. Demekhin, N. V. Nikitin, and V. S. Shelistov, Direct numerical simulation of electrokinetic instability and transition to chaotic motion, *Phys. Fluids* **25**, 122001 (2013).
- [45] C. L. Druzgalski, M. B. Andersen, and A. Mani, Direct numerical simulation of electroconvective instability and hydrodynamic chaos near an ion-selective surface, *Phys. Fluids* **25**, 110804 (2013).
- [46] M. K. Urtenov, A. M. Uzenova, A. V. Kovalenko, V. V. Nikonenko, N. D. Pismenskaya, V. I. Vasil'eva, P. Sistas, and G. Pourcelly, Basic mathematical model of overlimiting transfer enhanced by electroconvection in flow-through electro dialysis membrane cells, *J. Membr. Sci.* **447**, 190 (2013).
- [47] C. L. Druzgalski and A. Mani, Statistical analysis of electroconvection near an ion-selective membrane in the highly chaotic regime, *Phys. Rev. Fluids* **1**, 073601 (2016).
- [48] W. D. Ristenpart, P. Jiang, M. A. Slowik, C. Punckt, D. A. Saville, and I. A. Aksay, Electrohydrodynamic flow and colloidal patterning near inhomogeneities on electrodes, *Langmuir* **24**, 12172 (2008).
- [49] V. I. Zabolotsky, L. Novak, A. V. Kovalenko, V. V. Nikonenko, M. H. Urtenov, K. A. Lebedev, and A. Y. But, Electroconvection in systems with heterogeneous ion-exchange membranes, *Petroleum Chemistry* **57**, 779 (2017).
- [50] J. C. deValença, M. Jōgi, R. M. Wagterveld, E. Karatay, J. A. Wood, and R. G. H. Lammertink, Confined electroconvective vortices at structured ion exchange membranes, *Langmuir* **34**, 2455 (2018).
- [51] N. D. Pismenskaya, S. Mareev, E. V. Pokhidnya, C. Larchet, L. Dammak, and V. V. Nikonenko, Effect of surface modification of heterogeneous anion-exchange membranes on the intensity of electroconvection at their surfaces, *Russ. J. Electrochem.* **55**, 1203 (2019).
- [52] F. Roghmans, E. Evdochenko, F. Stockmeier, S. Schneider, A. Smailji, R. Tiwari, A. Mikosch, E. Karatay, A. Kühne, A. Walther, A. Mani, and M. Wessling, 2D patterned ion-exchange membranes induce electroconvection, *Adv. Mater. Interfaces* **6**, 1801309 (2019).
- [53] M. Seo, W. Kim, H. Lee, and S. J. Kim, Non-negligible effects of reinforcing structures inside ion exchange membrane on stabilization of electroconvective vortices, *Desalination* **538**, 115902 (2022).
- [54] E. Karatay, M. B. Andersen, M. Wessling, and A. Mani, Coupling between buoyancy forces and electroconvective instability near ion-selective surfaces, *Phys. Rev. Lett.* **116**, 194501 (2016).
- [55] J. C. deValença, A. Kurniawan, R. M. Wagterveld, J. A. Wood, and R. G. H. Lammertink, Influence of Rayleigh-Bénard convection on electrokinetic instability in overlimiting current conditions, *Phys. Rev. Fluids* **2**, 033701 (2017).
- [56] E. A. Demekhin, G. S. Ganchenko, and E. N. Kalaydin, Transition to electrokinetic instability near imperfect charge-selective membranes, *Phys. Fluids* **30**, 082006 (2018).
- [57] G. Li, A. Townsend, L. A. Archer, and D. L. Koch, Suppression of electroconvective and morphological instabilities by an imposed cross flow of the electrolyte, *Phys. Rev. Fluids* **6**, 033701 (2021).
- [58] I. Rubinstein and B. Zaltzman, The effects of reaction kinetics upon the instabilities in cathodic electrodeposition, *Curr. Opin. Colloid Interface Sci.* **60**, 101591 (2022).
- [59] S. Kim, M. A. Khanwale, R. K. Anand, and B. Ganapathysubramanian, Computational framework for resolving boundary layers in electrochemical systems using weak imposition of Dirichlet boundary conditions, *Finite Elem. Anal. Des.* **205**, 103749 (2022).
- [60] P. Shi, Direct numerical simulation of electroconvection with thin Debye layer matching canonical experiments, *Phys. Fluids* **33**, 032015 (2021).
- [61] E. Karatay, C. L. Druzgalski, and A. Mani, Simulation of chaotic electrokinetic transport: Performance of commercial software versus custom-built direct numerical simulation codes, *J. Colloid Interface Sci.* **446**, 67 (2015).
- [62] S. M. Davidson, M. Wessling, and A. Mani, On the dynamical regimes of pattern-accelerated electroconvection, *Sci. Rep.* **6**, 22505 (2016).
- [63] M. B. Andersen, K. M. Wang, J. Schiffbauer, and A. Mani, Confinement effects on electroconvective instability, *Electrophoresis* **38**, 702 (2017).
- [64] J. Kim, S. M. Davidson, and A. Mani, Characterization of chaotic electroconvection near flat inert electrodes under oscillatory voltages, *Micromachines* **10**, 161 (2019).



- [65] W. Liu, Y. Zhou, and P. Shi, Scaling relations in shear electroconvective vortices, *Phys. Fluids* **32**, 072009 (2020).
- [66] W. Liu, Y. Zhou, and P. Shi, Shear electroconvective instability in electro dialysis channel under extreme depletion and its scaling laws, *Phys. Rev. E* **101**, 043105 (2020).
- [67] V.-S. Pham and D.-A. Van, Numerical modeling for 3D vortices patterns of electroconvective flow developing in shear flow, *Phys. Fluids* **34**, 082016 (2022).
- [68] S. Cai, Z. Wang, L. Lu, T. A. Zaki, and G. E. Karniadakis, DeepM&Mnet: Inferring the electroconvection multiphysics fields based on operator approximation by neural networks, *J. Comput. Phys.* **436**, 110296 (2021).
- [69] Y. Guan, S. L. Brunton, and I. Novosselov, Sparse nonlinear models of chaotic electroconvection, *R. Soc. Open Sci.* **8**, 202367 (2021).
- [70] S. B. Pope, *Turbulent Flows* (Cambridge University Press, Cambridge, UK, 2000).
- [71] A. Kourmatzis and J. S. Shrimpton, Turbulence closure models for free electroconvection, *Int. J. Heat Fluid Flow* **71**, 153 (2018).
- [72] A. Mani and D. Park, Macroscopic forcing method: A tool for turbulence modeling and analysis of closures, *Phys. Rev. Fluids* **6**, 054607 (2021).
- [73] F. Hamba, Nonlocal expression for scalar flux in turbulent shear flow, *Phys. Fluids* **16**, 1493 (2004).
- [74] D. Park and A. Mani, Direct calculation of the eddy viscosity operator in turbulent channel flow at  $re_\tau = 180$ , [arXiv:2108.10898](https://arxiv.org/abs/2108.10898).
- [75] D. Park, J. Liu, and A. Mani, Direct measurement of the eddy viscosity tensor in a canonical separated flow: What is the upper bound of accuracy for local Reynolds stress models? in *Proceedings of the AIAA SCITECH 2022 Forum, San Diego, CA & Virtual* (AIAA, Reston, VA, 2022).
- [76] J. Liu, H. Williams, and A. Mani, Systematic approach for modeling a nonlocal eddy diffusivity, *Phys. Rev. Fluids* **8**, 124501 (2023).
- [77] A. Uzdenova, 2D mathematical modelling of overlimiting transfer enhanced by electroconvection in flow-through electro dialysis membrane cells in galvanodynamic mode, *Membranes* **9**, 39 (2019).
- [78] A. Uzdenova, A. Kovalenko, and M. Urtenov, Theoretical analysis of electroconvection in the electro dialysis desalination channel under the action of direct current, *Membranes* **12**, 1125 (2022).
- [79] E. Mattsson and J. O. Bockris, Galvanostatic studies of the kinetics of deposition and dissolution in the copper + copper sulphate system, *Trans. Faraday Soc.* **55**, 1586 (1959).
- [80] O. Brown and H. Thirsk, The rate-determining step in the electro-deposition of copper on copper from aqueous cupric sulphate solutions, *Electrochim. Acta* **10**, 383 (1965).
- [81] D. Deng, E. V. Dydek, J. H. Han, S. Schlumpberger, A. Mani, B. Zaltzman, and M. Z. Bazant, Overlimiting current and shock electro dialysis in porous media, *Langmuir* **29**, 16167 (2013).
- [82] J. R. Rumble (ed.), *CRC Handbook of Chemistry and Physics*, 104th ed. (Taylor & Francis Group, Boca Raton, FL, 2023).